LBL-36848
UC-400

Lawrence Berkeley Laboratory
UNIVERSITY OF CALIFORNIA

EARTH SCIENCES DIVISION

**Disturbed Zone Effects: Two Phase Flow in Regionally Water-Saturated Fractured Rock
FY94 Annual Report**

J.T. Geller, C. Doughty, J.C.S. Long, and R.J. Glass

January 1995

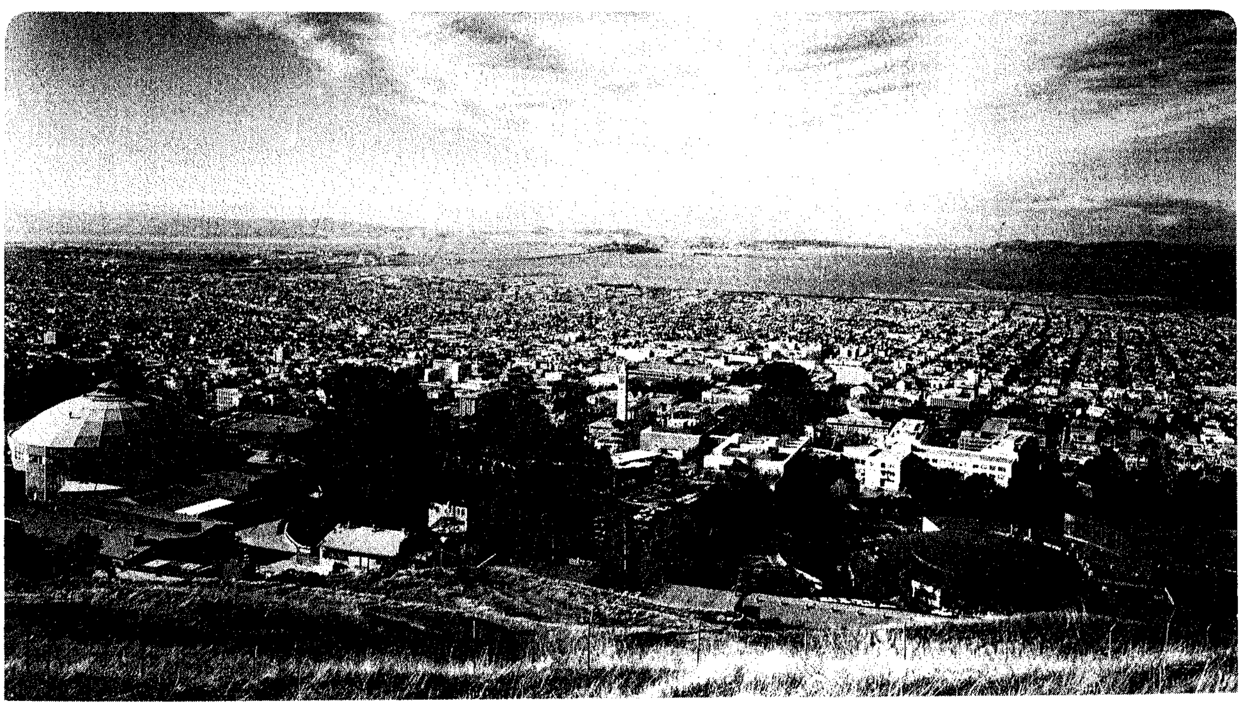

Prepared for the U.S. Department of Energy under Contract Number DE-AC03-76SF00098

DISCLAIMER

LBL-36848
UC-400

Disturbed Zone Effects: Two Phase Flow in Regionally Water-Saturated Fractured Rock

FY94 Annual Report to the International Program under the Cooperative Agreement between U.S. DOE and SKB (Swedish Radioactive Waste Management Company)

Jil T. Geller, Christine Doughty and Jane C.S. Long

Lawrence Berkeley National Laboratory
University of California
Berkeley, CA 94720

and

Robert J. Glass

Sandia National Laboratory, Albuquerque, NM 87185

January 1995

This work was carried out under U.S. Department of Energy Contract No. DE-AC03-76SF00098, for the Director, Office of Civilian Radioactive Waste Management, Office of External Relations, administered by the Nevada Operations Office and under the Swedish Nuclear Fuel and Waste Management Company (SKB) Contract NO. 268070. Numerical computations were supported by the Director, Office of Energy Research, Office of Basic Energy Sciences, Engineering and Geosciences Division, U.S. Department of Energy.

Contents

Disturbed Zone Effects: Two-Phase Flow

Abstract

Field evidence suggests that two-phase flow may develop near underground excavations in regionally-saturated fractured crystalline rock, resulting in lower inflow rates compared to undisturbed rock. Mechanisms for the development of two-phase flow conditions include depressurization of formation water that is supersaturated with dissolved gas and buoyancy-driven air invasion into fractures from the drift. Models that assume gas-liquid phase equilibrium indicate that for constant head boundary conditions, the build-up of pressure behind the gas phase evolving from depressurization should redissolve the gas and maintain higher flowrates, requiring unreasonably high dissolved gas concentrations to produce observed flow reductions at the Stripa Mine in Sweden. This discrepancy initiated a laboratory-scale investigation. Gas evolution following depressurization is simulated in two different 8 cm x 8 cm transparent fracture replicas for linear flow with constant head boundary conditions. Flow reduction due to gas evolution is the same order of magnitude as observed in the field. Gas forms and accumulates in the large apertures and the extent of flow reduction is greater when the flow through the fracture is controlled by a large aperture channel, compared to a fracture where large aperture regions are relatively isolated.

An effective continuum numerical model (TOUGH2) is used to describe the development of two-phase flow under degassing conditions. The model closely agrees with a simple analytical model; however, neither of the models predict the extent of flow reduction due to degassing observed in the field or laboratory. Numerical simulations were made for a homogeneous porous medium and for a heterogeneous medium using the aperture distribution of one of the fractures used in the laboratory experiments, which allows a direct comparison between laboratory and numerical results. Simulation in heterogeneous media shows that increasing the resolution of the smaller apertures achieves gas and mobility distributions that correspond with the experimental observations; however, actual gas saturations and total flow rate reduction due to degassing are not as high as observed experimentally. The slow dissolution rates of the evolved gas observed in the experiments has motivated an effort to incorporate mass transfer kinetics into the model.
The incorporation of kinetic expressions into the numerical model will allow the prediction of resaturation rates of a repository following closure.

Laboratory experiments of the dissolution of trapped air in roughened glass plates also raise questions regarding the validity of equilibrium assumptions between the bulk phases. The dissolution experiments show that the shrinkage of trapped air clusters is a complex interplay between mass flux at points of high liquid flow velocity and capillary forces that drive the recession of the gas-liquid interface. Experimental observations of air invasion into initially water-saturated roughened glass plates show that significant gas saturations are

achieved as buoyancy drives air fingers upward. Air invasion may be an important process for larger aperture fractures.

Field experiments are planned for the Hard Rock Laboratory in Äspö, Sweden, to test the hypotheses of flow reduction due to degassing. The experiments consist of a series of constant-pressure borehole inflow tests to observe the relationship between the steady-state inflow to the borehole and borehole pressure. Below the bubble pressure of the dissolved gas, a deviation from the linear relationship between borehole inflow and pressure would indicate the presence of two-phase flow conditions.

The interrelationship between the modeling, laboratory, and field components of this study provides the opportunity to test our fundamental understanding of two-phase flow in fractures and modify predictive models to reflect the important physical processes suggested by the field data and directly observed in the laboratory. This investigation will increase our confidence in two-phase flow predictions under the complex conditions occurring in fractured rock in other environments.

Part I. Background

A. Introduction

The investigation of potential underground nuclear waste repositories employs hydrologic testing from excavations that provide access to the subsurface with the purpose of characterizing flow systems in undisturbed rock. Effects of the excavation on the hydrologic response of the system must be understood so that the measured behavior can be extrapolated to the rock away from the drift. In an investigation of excavation effects in the Stripa Mine in Sweden, a regionally saturated granitic rock formation, flow rates into the drift were one order of magnitude lower compared to pre-excavation conditions (Olsson, 1992). An analysis of different factors that may have caused the flow disturbance, including stress changes, ventilation effects, blasting, chemical precipitation, and degassing of dissolved nitrogen due to exposure of the inflow boundary to near atmospheric pressure, concluded that the development of two-phase (gas and water) flow conditions following depressurization was a likely cause of flow reduction. Air invasion into fractures intersecting a drift, driven by buoyancy or blasting, is another potential mechanism for the development of two-phase flow conditions. Water evaporation and desaturation of the rock immediately surrounding the drift as a result of ventilation also disturbs the flow field in the near-drift region (Vomvoris and Frieg, 1991). Additional motivations for understanding two-phase flow phenomena in regionally saturated fractured rock relate to repository performance following waste emplacement (Davies *et al.,* 1993). The rate of repository resaturation, with its effect on the regional flow field and the potential of residual oxygen to corrode copper waste canisters designed for anaerobic conditions; transport of radionuclides via corrosion-generated gases; and the integrity of engineered backfill materials in the presence of the pressure build-up caused by gas generation also involve two-phase flow.

This progress report describes the theoretical analyses and laboratory experiments conducted to investigate the dynamics of two-phase flow phenomena in the near-drift region. The goals of the investigation are to establish the important mechanisms and conditions which promote two-phase flow conditions. The mechanisms considered here are gas phase formation as a result of depressurization and buoyancy-driven air invasion. The dominant mechanisms are likely to depend upon the type of fractures and dissolved gas contents of the water. The evolution of a gas phase following depressurization of gas-saturated water is studied for constant head boundary conditions. This process is described analytically and numerically using an effective continuum model. Laboratory experiments are conducted to assess the importance of physical-chemical processes not currently described by the theoretical models. An analysis of buoyancy-driven air invasion from the drift and supporting laboratory experiments show that this mechanism may be important for larger-aperture fractures. This work will support the demonstration of mechanisms at a field test at the Hard Rock Laboratory in Äspö, Sweden.

B. Development of Gas Phase

Gas-Liquid Phase Equilibria. Dissolved gas contents in water-saturated formations vary greatly. Henry's Law describes the equilibrium of a species between the gas and liquid phases as follows:

$$y_a P_T = H x_a \qquad \text{(I.1)}$$

where y_a is the mole fraction of species a in the gas phase, P_T is the total pressure, H is the Henry's Law constant and x_a is the mole fraction of species a in the liquid phase. The product $y_a P_T$ is the partial pressure of species a. H is a function of temperature and salinity.

It follows from Equation I.1 that the bubble pressure P_B, or the pressure at which a liquid containing a given amount of gas is saturated, is given by:

$$P_B = H x_a \qquad \text{(I.2)}$$

If a liquid containing an amount x_a of gas is at a pressure $P > P_B$, then the gas will remain dissolved in the liquid phase. On the other hand, if the pressure is lowered to $P < P_B$, then a separate gas phase will form as the gas comes out of solution, a process known as degassing. Henry's law assumes chemical equilibrium between the gas and liquid phases, and does not incorporate the kinetics of degassing and dissolution.

Equation (I.1) can be used to estimate the dissolved gas concentrations at Stripa, where gas bubbles were observed in the borehole after the borehole pressure was reduced from 800 to 270 kPa (abs) (Olsson, 1992). Reported values of total dissolved gas contents in Stripa waters ranged from 2 to 4%, where over 95% of the gas was nitrogen (Olsson, 1992). Using a value of H equal to 6.67 x 10^3 MPa(mole fraction)$^{-1}$ for nitrogen in distilled water at 10°C (International Critical Tables, Vol. III), equation (I.1) predicts a gas content of 5.3% v/v @ STP for a bubble presure of 270 kPa (abs).

This value represents the total amount of dissolved gas in the water and will be referred to as total gas contents. The amount of dissolved nitrogen in water at atmospheric pressure, calculated from equation (I.1) using H = 6.67 x 10^3 mPa (mole fraction)$^{-1}$ is 1.9% v/v @ STP. Substracting this value from the total gas contents provides an estimate of the volume of gas per volume of water that evolves when the formation water pressure is reduced to atmospheric pressure.

Bubble Trapping. If the gas that comes out of solution becomes trapped in the fractures and accumulates, significant flow blockage may occur. The pressure difference across a gas-liquid interface trapped by a restriction formed by two parallel plates separated by a distance b is equal to:

$$\Delta P_{g-l} = \frac{2\sigma \cos\theta}{b} \tag{I.3}$$

where σ is the surface tension of the liquid and θ is the contact angle of the water with the solid surface, measured through the water phase. The pressure arising from viscous forces on the bubble is proportional to the prevailing gradient dh/dl multiplied by the bubble length L_b. Assuming horizontal flow with no buoyancy effects, the bubble length that would be pushed through a restriction by the prevailing gradient is then equal to:

$$L_b = \frac{\Delta P_{g-l}}{(dh/dl)\,\rho_l g} \tag{I.4}$$

where ρ_l is the liquid density and g is the acceleration of gravity. Bubbles having lengths less than L_b would be trapped. This calculation neglects compressibility and drag forces along the bubble walls; however, it illustrates the size of bubbles and apertures where trapping may occur. Figure I.1 plots L_b as a function of restriction opening, b, for gradients of 1 and 10, assuming θ equals zero and σ equals the surface tension of pure water, 73 mN m^{-1}. When the bubble length is less than b, below the solid line in Figure I.1, the bubble is spherical and passes through the restriction. Above the solid line, the bubble is no longer spherical and could become trapped. Figure I.1 shows that at a gradient of 1, a 1-mm restriction can trap 10 mm long bubbles and a 0.1 mm restriction can trap bubbles up to 100 mm long. Hydraulically significant fractures often have apertures less than 1 mm, indicating that conditions for bubble trapping exist.

<u>Buoyancy-Driven Air Invasion</u>. The analysis in the previous section can also be used to illustrate the potential for buoyancy-driven air invasion into a fracture intersecting the drift. In this case, the driving force for bubble movement is the difference between the density of air and water, so that for stagnant water in a vertical fracture, the minimum bubble length required for air invasion is:

$$L_b = \frac{\Delta P_{g-l}}{(\rho_l - \rho_g)g} \tag{I.5}$$

where ρ_g is the density of the gas phase or air. Equation I.4 reduces to Equation I.5 for ρ_l >> ρ_g and when the gradient equals 1. For air invasion (mobilization), the bubble length for a given restriction is greater than or equal to the value in Figure I.1, *e.g.*, bubbles having a vertical length of 10 mm or greater will rise through a vertical fracture with a restriction of 1 mm. As the restriction opening increases, the bubble length for air invasion decreases, illustrating that this mechanism becomes more important in larger aperture fractures.

Gas Phase Evolution Following Depressurization. The processes involved in the formation of a gas phase following depressurization has received some attention in the petroleum engineering literature with regard to the solution gas-drive process (e.g. Firoozabadi and Kashchiev, 1993; Parlar and Yortsos, 1989). The solution gas-drive process is a mechanism that enhances oil recovery from fractured and unfractured reservoirs, where a gas phase forms when the pressure is lowered below the bubble pressure of the volatile components. Up until the point where the gas phase becomes continuous and mobile, called the critical gas saturation, the expanding gas phase enhances oil recovery. The formation of the gas phase begins with nucleation, where clusters of molecules within one phase formed by collisions attain a size that is energetically favorable for growth of the second phase. This is a non-equilibrium process and requires a certain degree of supersaturation to occur. The presence of the porous medium significantly affects the mechanisms of.nucleation and the subsequent growth of the gas phase. The availability of rough surfaces in porous media promotes conditions for hetrogeneous nucleation where bubbles arise from sites on pore walls containing trapped gas (either pre-existent or nucleated), which is released (i.e. sites become activated) when local supersaturation is reached, as compared to homogeneous nucleation occurring in pure bulk fluids (Parlar and Yortsos, 1989).

Bubble growth is driven by both diffusion of gas molecules across the gas/water interface and expansion as the surrounding liquid pressure decreases. Li and Yortsos (1991) observed bubble growth from CO_2-saturated water in a glass micromodel during constant rate pressure reduction. The micromodel had regular square lattice patterns of sizes ranging from 0.1 to 1 mm. They observed the growth of clusters in ramified structures from nucleation sites activated at different stages of pressure reduction. Rapid bubble growth occurred after nucleation at the pore wall and bubble detachment towards the center of the pore was also observed. In a Hele Shaw cell with a spacing of 0.2 mm, bubble growth was almost perfectly radial at early stages; bubbles formed from different sites coalesced. Within fractures, one may expect growth patterns to be intermediate between the two.

Gas Phase Dissolution. Henry's law assumes chemical equilibrium between the gas and liquid phases. Consequently, if gas blocks a flow path and pressure builds up behind the gas, Henry's law predicts that the gas will dissolve. Equilibrium requires good contact between the phases, either by mixing or extremely large specific surface areas (area to volume ratios) or by long contact times. Equilibrium conditions may occur at the gas-liquid interface, however diffusion of the dissolved gas to and from the interface may limit mass transfer. The laminar flow conditions in groundwater preclude good mixing between fluid phases. Surface area between the phases may limit interphase mass transfer. As discussed in the previous section, the gas phase initially evolves as small bubbles having large specific surface areas; however the subsequent transport, trapping and accumulation of the bubbles reduces the specific surface area, as well as the surface area in contact with the flowing water. Consequently, the rate of dissolution of the evolved gas may occur much more slowly than the rate of gas phase formation.

Two-Phase Flow. Our present conceptual model for two-phase flow through fractured rock uses an effective continuum approach, in which fluid flow through the fractures is assumed to be governed by Darcy's law. Mass balances are formulated at the scale of aperture variations in the fracture plane, in order to allow for heterogeneity in the flow domain. This scale is typically much greater than bubble nucleation size; hence, individual bubble population balances are not done. Instead, if a region contains both gas-phase bubbles and liquid-phase water, Darcy's law is applied to each phase separately, with relative permeability and capillary pressure curves used to describe the interference and interaction between phases.

Part II. Laboratory Studies

A. Degassing

Rationale. Analytical and numerical models indicate that much higher gas contents than those occurring at Stripa would be required to produce the flow reductions observed due to degassing. The purpose of the laboratory experiments is to demonstrate whether degassing can cause the magnitude of flow reductions observed in the field under controlled conditions and to assess whether the models incorporate the relevant physical processes.

Experimental Apparatus. The laboratory experiments simulate the development of two-phase flow conditions following depressurization in transparent fracture replicas for linear flow geometry with constant boundary pressure conditions. Carbon dioxide is used as the dissolved gas because of its relatively high solubility in water; its Henry's Law constant is 1.15×10^2 MPa(mole fraction)$^{-1}$. Figure II.A.1 describes the layout of the apparatus. Constant influent and effluent pressures are maintained with a Mariot tube in the influent vessel and an overflow tube in the outlet vessel. Distilled water and CO_2 gas are equilibrated in the influent vessel by injecting CO_2 through a frit in the bottom of the reservoir at the desired pressure. Additional pressure to drive flow is applied with N_2 gas through the Mariot tube. Effluent pressure is controlled by the elevation of the outlet reservoir or by application of N_2 gas to the outlet vessel to achieve higher pressures. All gas pressures are controlled with pneumatic pressure regulators that operate over an absolute pressure range of 107 to 400 kPa (Fairchild Industrial Products Co., Winston-Salem, NC, model 65A). Either deaired or CO_2-saturated water flows from the influent vessel through a needle valve, followed by a 0.5 μm filter (Nupro, TF), then a variable-area flowmeter (Gilmont, Cole Parmer Instrument Co., Chicago, IL), through the fracture and into the outlet vessel. Flowrates indicated by the variable-area flowmeter are recorded with a video camera. The purpose of the filter on the upstream side of the fracture is to prevent clogging of the fracture with particulates. Differential pressures across the fracture, and absolute pressures at the fracture inlet and outlet, are continuously monitored with pressure transducers (Validyne DP15, Northridge, CA) with a signal conditioner (Validyne CD18, Northridge, CA) and acquired to a PC. The pressure taps have a ceramic disc with an air entry pressure of 200 kPa which directly contact the fracture face to prevent gas from entering the lines to the pressure transducers.

The transparent replicas allow the direct observation of the gas and liquid phase distributions during the experiment, a technique used by Persoff and Pruess (1993) and Nicholl *et al.* (1994). The experiment is mounted over a light table, and observations of gas and liquid phase distributions within the fracture plane are recorded with video photography. Digitized images are acquired with a frame-grabber (Data Translation 2871, Marlboro, MA). Because water matches the refractive index of the epoxy more closely than it does gas, water-occupied spaces transmit light better and appear brighter. The curved surfaces of bubbles appear dark. The replicas are clear, 7.6 x 7.6 cm, epoxy resin (Ecobond 27, Emerson and Cuming, Canton, MA) casts of both sides of a natural, rough-walled rock fracture. The contact angle of water on the smooth epoxy surface is 70° measured through the water by the captive drop method as described in Adamson (1982). The experiments reported here utilized two fracture replicas whose aperture distributions have been characterized previously by light attenuation (Persoff *et al.*, 1991; Persoff and Pruess, 1993). The Dixie Valley sample is a faulted rock fracture from a geothermal area in Nevada. The Stripa sample is from a horizontal fracture in granite rock core from the Stripa mine in Sweden. The fracture replica is compressed between two lucite blocks that are 10 cm thick to a stress of approximately 30 kPa. For the Dixie Valley fracture, two types of endcaps were used. The first type of endcap was filled with a ceramic piece having an air entry pressure of 200 kPa that was in contact with the fracture and served to distribute and collect flow across the fracture inlet and outlet. A pair of narrow bars compressed rubber gaskets along the top and bottom edges of the inlet and outlet sides which sealed the fracture. Both the ceramic and sealing bars caused some problems which will be discussed later, so subsequent tests were conducted with endcaps that allowed a 2 mm deep void along the fracture inlet and outlet for flow distribution and collection. Tests conducted with the ceramic endcaps are referred to as Dixie Valley I and tests conducted with the void endcap are called Dixie Valley II. For the Stripa fracture, only the endcap with the void was used.

Aperture maps of the two fractures are shown in Figures II.2(a) and (b), after Cox and Wang (1993). The white regions represent apertures that are greater than 50 μm. Direction of flow is from right to left. The Dixie Valley fracture is characterized by strong striation in the direction of flow and some larger aperture areas in the middle and upper left hand corner. The Stripa fracture has a large aperture channel that extends from the upper left hand corner down the fracture and towards the right hand side.

Experimental Procedures. Initially the hydraulic conductivity of each fracture was measured for fully water-saturated conditions using deionized, deaired water. From the slopes of the Q vs ΔP lines, the effective hydraulic aperture, b, is computed as follows:

$$b = (12kh)^{1/3} \qquad \text{(II.1)}$$

where k is the permeability and h is the effective height of the fracture. The term kh is evaluated from Darcy's Law:

$$Q = \frac{kh}{\mu} \frac{\Delta P}{L} w \qquad \text{(II.2)}$$

where Q is the volumetric flowrate, μ is the liquid viscosity, ΔP is the differential pressure from fracture inlet to outlet, L is the length of the fracture edge from inlet to outlet, and w is the width of the fracture edge at the inlet. The values of the hydraulic aperture are 9.37, 18.8 and 12.8 μm for Dixie Valley I, II and Stripa fractures, respectively. The difference between Dixie Valley I and II is attributed to the bars that seal the top edges of the fracture which apparently compress the fracture near the inlet and outlet more than the lucite block.

After hydraulic conductivity is measured for water-saturated conditions, the fracture is saturated with dyed, deaired water. The dyed water is a solution of 1% Liquitint Patent Blue (Milliken Chemical, Inman, SC) in distilled water. The water in a second inlet vessel is saturated with CO_2 gas at the desired bubble pressure, which will henceforth be referred to as the partial pressure of CO_2, or P_{CO_2}. The water and CO_2 are equilibrated for a minimum of 24 hours. The inlet vessel is pressurized with N_2 to a pressure above P_{CO_2} to initiate the flow of the CO_2-saturated water through the fracture while the effluent pressure is maintained above the bubble pressure, displacing the dyed, deaired water. Once the fracture is clear, indicating that it is saturated with water containing dissolved CO_2, the effluent pressure is reduced to below P_{CO_2}. Experiments are conducted until flowrates and gas saturations no longer vary with time.

Table II.1 summarizes the conditions of the experiments. Between DVIa and b, the fracture was resaturated without disassembly by increasing the outlet vessel pressure to 129 kPa (abs). The experiment with the Stripa fracture, S-a, was conducted in accordance with the procedures in the preceding section. After steady-state was reached, the boundary conditions were changed in S-b and S-c.

Results. Figures II.A.3 through II.A.6 show the pressure and flow data for the DVIa, DVIb, DV II, and Stripa experiments. In the first experiment, DVIa, the outlet pressure regulator malfunctioned, causing pressure fluctuations over the first 16 hours; at times the outlet pressure dropped below P_{CO_2}. Gas was observed in the flowmeter and fracture at t = 18 hours; from that time on, flowrates declined until flow stopped entirely. The decline of the fracture inlet pressure beginning at t = 18 hr indicates that gas upstream of the fracture and not in the fracture itself was blocking flow. The gas phase may have formed downstream of the flow control valve, causing blockage upstream of the filter or upstream of the ceramic endcap. To reinitiate flow, the inlet and outlet vessel pressures were increased and decreased, respectively, to the values shown in Table II.1. This eventually established constant pressure boundary conditions and over this time period the flowrate increased very slowly, until reaching a steady value, at which point the experiment was stopped. The final value of 3 mL/h is four times lower than the flowrate of 12 mL/h that would be expected for water-saturated conditions, as predicted by the hydraulic conductivity measurements.

Table II.1. Summary of experimental conditions and results

Experiment	P_{CO_2} (kPa) (absolute)	P_{infl} (kPa)	P_i (kPa)	P_o (kPa)	% gas[6]	P*	q/q_o
DVIa[1]	129	163	159	113	14.8	0.32	0.28
DVIb[1,2]	118.5	156	154	106	11.6	0.25	0.23
DVII[3]	118.5	128	102	93	23.6	0.73	0.20
S-a[3]	118.5	136	133	111	7.0	0.30	0.08
S-b[3,4]	118.5	136	133	104	13.4	0.45	0.05
S-c[3,5]	118.5	148	147	104	13.4	0.33	0.04

Notes:

1. Ceramic endcaps.
2. Following resaturation of DVIa without disassembling fracture
3. Endcaps with 2 mm void.
4. Boundary conditions were changed following steady-state conditions in S-a
5. Boundary conditions were changed following steady-state conditions in S-b
6. Percent by volume at 20°C and 101.3 kPa, evaluated according to equation (II.3)

The next experiment, Dixie Valley Ib, was conducted after resaturating the fracture with deaired, dyed water, for a lower P_{CO_2} value of 118.6 kPa (abs). As in DVIa, gas appeared in the fracture while the outlet pressure was higher than P_{CO_2}. It appears that the initial gas came from residual gas trapped in the porous ceramic endplate and not upstream of the fracture because the inlet pressure did not decrease as gas evolved, and no gas was observed in the flowmeter. Increasing the inlet vessel pressure and decreasing the outlet vessel pressure caused flow to resume and a pattern similar to the first experiment was observed of gradual flowrate increase with an increase of water saturation along the inlet side of the fracture. The final flowrate of 2.6 mL/h is approximately four times lower than the water-saturated flowrate of 12 mL/h.

In the next experiment, DVII, the fracture was successfully saturated with water containing dissolved CO_2, which provided an opportunity to observe gas evolution with depressurization under no-flow conditions. Pressure was relieved by opening the outlet vessel to the atmosphere with the influent pressure vessel valve closed to prevent flow through the fracture. Because the elevation of the effluent pressure vessel was below that of the fracture, the actual pressure in the fracture was 88.9 kPa (abs). The formation of a few small gas bubbles within the large aperture regions of the fracture was observed during the first 40 minutes following depressurization, however beyond this time no further gas appeared in the fracture. Gas also formed in the inlet and outlet tubing. Once flow began, the initial gas bubbles grew, apparently as the flowing water delivered gas to those sites. Bubbles were also observed in the flowmeter upstream of the fracture, indicating that as water flowed, the gas phase formed between the inlet vessel and the flowmeter. By the end of the experiment, flowrates in the presence of the gas phase were lower by a factor of 6 compared to the water-saturated conditions, although the inlet end did not resaturate as in DVIa and DVIb.

The last experiment was conducted with the Stripa fracture, using the same endcap arrangement as in Dixie Valley II. Fracture inlet and outlet pressures were kept above the bubble pressure when injecting the CO_2-saturated water, however during this time gas appeared in the flowmeter and fracture. Some gas may have formed from residual gas in the ceramic filter, but the occurrence of bubbles in the flowmeter was much lower than in the Dixie Valley experiments. This observation, along with the fact that gas appearing in the fracture is not connected to the inlet side indicates that most of the gas in the fracture did come out of solution in the fracture and not upstream of the fracture. Once gas appeared, flowrates decreased. Following a decrease in outlet pressure, more gas appeared in the fracture, and flowrates continued to drop. This secondary decrease in flowrates was much smaller than the initial drop when gas first appeared, presumably because the flow blocking was due in large part to the gas on the outlet side of the fracture which did not change. A subsequent decrease in effluent pressure also resulted in a drop in flowrates. The two changes in outlet pressures below the bubble point give flow reductions by factors of 12 and 20 respectively. Finally, the inlet pressure was increased, which produced a flow reduction factor of 25.

Discussion. Table II.1 summarizes the experimental results. The percent of gas is the volume of gas per volume of liquid at 20°C and 1 atm pressure (101.3 kPa) that evolves based upon the difference between P_{CO_2} and the pressure at the fracture outlet, P_0 computed as follows:

$$\frac{V_{gas}}{V_{H_2O}} = \frac{\left(P_{CO_2} - P_0\right)}{H}\left(\frac{\bar{v}_{gas}}{\bar{v}_{H_2O}}\right) \tag{II.3}$$

where H is Henry's Law constant, and $\bar{v}_{gas}$ and $\bar{v}_{H_2O}$ are the molar volumes of gas and water, respectively. P^* is an expression for the bubble pressure normalized by the boundary pressures as follows:

$$P^* = \frac{P_{CO_2} - P_0}{P_1 - P_0} \tag{II.4}$$

such that a higher value of P^* corresponds to more gas in the fracture. Also, as P^* increases, gas comes out of solution closer to the inlet boundary and a larger fraction of the fracture length should be occupied by gas. The ratio q/q_0 represents the measured flowrate at the given value of P^* divided by the flow that would occur for the same pressure gradient under water-saturated conditions. The water-saturated flowrate is computed from the measured transmissivity of the fracture (equal to kh), using Darcy's Law (equation II.2).

The results are plotted in Figure II.A.7, along with the values from the Stripa SDE. The laboratory values for the normalized flow, q/q_0, are within the same range observed in the field. This provides strong evidence that degassing under constant boundary conditions can cause significant flow reductions. Flowrate reduction due to degassing has a slight dependence upon gas content, but the more significant differences occur between the two fractures, where over the same range of values of normalized bubble pressure, the flow reduction in the Stripa series is 5 times greater than in the Dixie Valley series. The reason for the difference can be seen in Figure II.A.8, which shows the steady-state gas distributions in the two fractures (DVIb and S-c), compared with their aperture maps. Flow direction is right to left. In Figure II.A.8.a, white indicates the gas phase; in Figure II.A.8.b, white indicates the large aperture regions (greater than 50 μm). The correspondence between the white regions shows that the gas resides in the large apertures of the fractures. In the Stripa fracture, the left hand side of the fracture was outside the field of view of the camera; however, the aperture distribution shows the entire fracture. The gas phase continues throughout the large aperture channel which extends across the fracture, resulting in a greater blockage to liquid when compared with the Dixie Valley fracture, where the large aperture regions are disconnected.

Conclusions. The experiments show that degassing under constant pressure boundary conditions can produce the magnitude of flow reductions observed in the Stripa Simulated Drift Experiment. The extent of flow reduction is very sensitive to fracture geometry and less sensitive to gas content, because flow blockage occurs as gas accumulates in the large aperture regions.

B. Dissolution of Entrapped Air and Air Invasion
(R.J. Glass, Sandia National Laboratory)

Introduction. Laboratory experiments to observe flow behavior during dissolution of an entrapped gas phase were conducted at Sandia National Laboratory. A summary of these experiments follows; the reader is referred to Glass and Nicholl (in press) for a complete report of this work. This section also includes a brief description of preliminary experiments to observe the formation of two-phase flow conditions as a result of air invasion.

Experimental System. Two roughened glass plates (30x15 cm) are held in close contact to form a rough walled analog fracture. No-flow boundaries are implemented on the long sides of the fracture; depending on the experiment, either constant flux conditions or no-flow/evaporative conditions are implemented on the short sides of the fracture.

The transparent analog fracture allows collection of phase structure data through the use of digital imaging techniques. The transparent test cell is placed on a rotating test stand that is back lit with high-frequency fluorescent lamps. Data is acquired through use of an imaging system focused on the fracture plane; the imaging system is capable of obtaining data at 2048 x 2048 pixels of spatial resolution with a dynamic range of 4096 gray levels. In order to enhance contrast, the experimental fluid is dyed blue, using a mixture of 1 g FD&C blue

#1 to 1 liter of de-ionized water. Simple light absorption theory is used to characterize both the aperture field and phase occupancy, thereby allowing measurement of phase saturation (S) under partially saturated conditions. (See Nicholl et al. (1994) for details of experimental system.)

Entrapped Air Dissolution Experiment. Starting with a saturated fracture, water was slowly displaced by air leaving a complicated entrapped water structure. Water flow was then established yielding a connected water structure and complicated entrapped air structure within the flowing fracture. Steady state water flow was then switched to degassed water and the differential head across the fracture was monitored. Over the next 24 hours, images of the wetted structure and differential head across the fracture were measured as the entrapped air dissolved into the water. At hourly increments, dye pulses were automatically delivered and imaged to visualize the channeling/tortuosity imparted by the entrapped air phase on solute transport.

The wetted structure at incremental times was summed to yield a composite image of gas structure solution as a function of time, shown in Figure II.B.1. The effects of the entrapped gas structure on solute transport are dramatic. Figure II.B.2 shows an image of the relative concentration field calculated using light adsorption theory. Effects on relative permeability are equally dramatic; the initial entrapped gas structure produces a drop in the permeability by a factor of eight. Fracture relative permeability as a function of water-phase saturation showed a smooth power law behavior during dissolution. Concentration fields were used as a surrogate for dissolved gas concentrations near entrapped gas to identify locations of high mass transfer rates. Locations for the advance of the wetting phase (water) into a nonwetting entrapped air cluster upon its dissolution were not always correlated with either zones of high mass transfer rate or with narrow apertures where the wetting phase has been thought to most easily invade. These results suggest that within an individual cluster of the entrapped phase, fluid pressure is at equilibrium and that the path of cluster shrinkage may be controlled primarily by capillary forces resulting from the full three-dimensional curvature that minimizes surface energy of the phase interface.

Gravity-Driven Instability: Vertical Fracture Drying from Below. The rough glass plate analog fracture was saturated and sealed at one end. The fracture was placed on the rotating test stand in a horizontal orientation. The test stand was then rotated to the position chosen for the experiment with the sealed end of the fracture at top. Water from the fracture was then allowed to evaporate from the bottom surface. Over a period lasting from a day up to a week, images were taken to track the evolution of the drying front as it moved into the fracture.

When the fracture was near horizontal, drying of the fracture proceeded very slowly with a complicated drying front evolving as a function of time. For fracture orientations where the top of the fracture was at a height above the lower boundary greater than the difference between the air entry value and the water entry values of the hysteretic pressure potential/saturation curve (L_C) for the fracture, gravity-driven air/water interfacial instability occurred causing the formation of upward growing finger structures. When the finger acquired a vertical length of L_C or greater, the finger began to move rapidly upward to the top of the fracture leaving a trail of entrapped air in its wake. Figure II.B.3 shows a composite image of the growing fingers averaged over a number of transient fingering events.

Part III. Modeling Studies

A. Introduction

Modeling of the degassing/dissolution process began with a simple conceptual model which yielded an analytical solution for flow reduction due to degassing. It greatly underpredicted the flow reduction observed at Stripa and in laboratory experiments conducted at LBL on fracture replicas. Subsequently we relaxed some of the assumptions made for the original conceptual model, to see if a greater flow reduction due to degassing could be predicted. This required replacing the analytical solution with numerical simulations to predict flow reduction. The modifications to the conceptual model are described below, along with their effect on the degassing process in general and on the magnitude of flow reduction in particular. Because no significant enhancement in flow reduction has been achieved, further model development is planned.

We assume that the fluid flow rate through a fractured or porous medium may be described by Darcy's law:

$$q = q_l + q_g = -\left[\frac{\rho_l k_{rl}}{\mu_l} + \frac{\rho_g k_{rg}}{\mu_g}\right] k \nabla P \qquad \text{(III.1)}$$

where the subscripts l and g denote liquid and gas phases, respectively; q is mass flow rate per unit area; ρ is density; μ is viscosity; k_r is relative permeability of a phase, which increases as phase saturation increases; and k is intrinsic permeability. The functional dependence of k_{rl} and k_{rg} on saturation is poorly known for many geologic media, especially for fractured systems. In order for degassing to cause a significant decrease in flow, as observed at Stripa, it appears that two effects must occur. First, the decrease in liquid saturation accompanying degassing must greatly decrease k_{rl}. Secondly, the gas bubbles themselves cannot be very mobile or they would rapidly flow out to the drift, again leaving liquid-phase conditions in the rock. Thus small gas saturations must result in very low values of k_{rg}. Together, these two effects describe a situation in which the two fluid phases exhibit strong phase interference, which is exactly the situation expected for flow through poorly connected fracture networks.

B. Simple Analytical Solution

We first consider a very simple geometry, in order to isolate the effects of degassing on fluid flow. We consider one-dimensional flow through a uniform medium of length L, to a constant pressure boundary, P_0, which represents a drift. We treat the linear-flow case first, then generalize to the other cases. The medium could represent a single fracture or a section of fractured rock matrix with enough fractures to be considered an effective medium, characterized by only a single value of permeability.

To complete specification of this simple flow problem, we need to apply a boundary condition at the end of the medium that is not at the drift. There are three possibilities:

A Semi-infinite system ($L \to \infty$)

B Closed system (no flow at $x = L$)

C Constant pressure P_1 at $x = L$

Of these three cases only Case C leads to a steady-state solution with a non-zero flow rate into the drift, which was observed at Stripa, so it will be used.

We consider the case in which $P_0 < P_B < P_1$, so that there are two-phase conditions at the drift ($x = 0$) and single-phase liquid at $x = L$. We define l as the distance from the drift at which pressure equals P_B. Under steady-state conditions, if there were no degassing, the flow to the drift could be obtained by integrating Equation III.1 to obtain

$$q_0 = -K_l \frac{P_1 - P_0}{L} \qquad \text{(III.2)}$$

where $K_l = \rho_l k / \mu$, since $k_{rl} = 1$ and $k_{rg} = 0$. If degassing occurred but did **not** affect k_{rl} or k_{rg} significantly, this solution would also apply. If degassing does affect k_{rl} and k_{rg}, then for $0 < x < l$, steady-state flow into the drift is given by

$$q = -\left[\frac{\rho_l k_{rl}(S(x))}{\mu_l} + \frac{\rho_g k_{rg}(S(x))}{\mu_g}\right] k \nabla P(x) \qquad \text{(III.3)}$$

For $l < x < L$, where $P > P_B$, and liquid phase conditions prevail we have

$$q = K_l \frac{P_1 - P_B}{L - l} \qquad \text{(III.4)}$$

The upper frame of Figure III.1 shows the steady-state pressure distributions schematically. To determine l and thus solve the problem exactly, we would need to know functional forms for k_{rl} and k_{rg}, but to find just a lower limit on q (that is, the maximum flow reduction that could take place) we can make the following approximation. Assuming that phase interference is very strong, a very sharp pressure gradient is required to drive any flow through the two-phase regime. This means that the value of l will be very small, as shown in Figure III.1. If we take $l \approx 0$, we get

$$q = -K_l \frac{P_I - P_B}{L} \tag{III.5}$$

and the normalized flow (defined as q / q_0) becomes simply

$$\frac{q}{q_o} = \frac{P_I - P_B}{P_I - P_o} \tag{III.6}$$

which holds for $l << L$. This relationship is plotted in the lower frame of Figure III.1. Note that this maximum flow reduction is independent of the length L of the medium, as well as the details of the relative permeability curves (as long as phase interference is strong).

Completely analoguous calculations can be made for radial or spherical flow geometry. For radial or spherical geomertry with no degassing, steady-state liquid-phase flow is given by

$$q_0 = -K_l \frac{P_I - P_0}{ln(r_I / r_0)} \qquad \text{radial}$$

(III.7)

$$q_0 = -K_l \frac{P_I - P_0}{(1/r_0) - (1/r_I)} \qquad \text{spherical}$$

Where r_I and r_0 are the distances at which pressure is held fixed at P_I and P_0, respectively. If we assume that under degassing conditions, $P = P_B$ at a distance r_B, then for $r_B < r < r_I$

$$q = -K_l \frac{P_I - P_B}{ln(r_I / r_B)} \qquad \text{radial}$$

(III.8)

$$q = -K_l \frac{P_I - P_B}{(1/r_B) - (1/r_I)} \qquad \text{spherical}$$

As in the linear-geometry case, assuming that $r_B \approx r_0$ and dividing Equation III.8 by III.7 allows all spatial dependence to drop out of the expression for q / q_0, so Equation III.6 holds independent of flow dimensionality.

Figure III.1 illustrates that to get a significant flow reduction (i.e., a small value of q / q_0), P_B must be much closer to P_1 than to P_0. The importance of P_B arises from the equilibrium assumption on degassing and dissolution. The pressure gradient near the borehole increases in response to the decreased relative permeability caused by degassing. As pressures rise above P_B, gas is driven back into solution, thus limiting the ability of the degassing process to reduce flow.

Verification of the Analytical Solution. The numerical model TOUGH2 was used to model the problem described by Case C, in order to investigate the accuracy of the analytical solution. TOUGH2 (Pruess, 1987, 1991) is a numerical simulator that calculates multiphase flow of air and water and heat transport through porous or fractured media. For the present problem nitrogen gas replaces air, and isothermal conditions are assumed.

Figure III.2 illustrates the steady-state conditions arising from a TOUGH2 calculation for a medium initially filled with liquid with a total gas content of 5.5%. The van Genuchten (1980) relative permeability functions were used with $\lambda = 0.5$, where λ describes the extent of phase interference. Capillary pressure, defined as the difference between liquid- and gas-phase pressures, is assumed to be negligible. Boundary pressures are $P_1 = 500$ kPa and $P_0 = 100$ kPa; the initial pressure is P_1 throughout the medium. The linear pressure profile that would occur without degassing is also shown, as is the value of P_B (312 kPa). Note that k_{rl} decreases much more than S_l, corresponding to the steepening of the pressure profile for $P < P_B$. The normalized flow is $q / q_0 = 0.62$. Figure III.3 quantifies the effect of λ, and shows that as λ decreases, signifying greater phase interference, the pressure profile indeed approaches that of the approximate analytical solution ($q / q_0 = 0.47$). Figure III.4 shows the effect of including a non-zero capillary pressure. Now in the two-phase region, the liquid and gas-phase pressures are different, and are related by $P_{cap} = P_l - P_g$, where capillary pressure is prescribed as a function of liquid saturation, using the van Genuchten (1980) formulation. Henry's law uses gas-phase pressure, P_g to calculate the amount of dissolved gas present. However, Darcy's law uses liquid-phase pressure P_l to calculate liquid flow. The net effect of including capillary pressure is to increase the pressure gradient for $P > P_B$, and thus increase the normalized flow ($q / qo = 0.83$ as compared to 0.62 with no capillary pressure).

Discussion. The preceding simple calculations have indicated that for the quoted conditions of the Stripa experiment, a total gas volume of approximately 3-6%, degassing is unlikely to have accounted for the observed normalized flow of 0.11, suggesting that some physical processes or boundary conditions are being incorrectly modeled. To do a more accurate calculation, more realistic boundary conditions and characteristic curves (relative permeability and capillary pressure functions) are needed. In addition, it is probable that a heterogeneous fractured/porous model will be needed. Use of such a model requires even more information on characteristic curves, as the interplay between fracture and matrix can become a dominant factor in controlling flow. If non-equilibrium effects are found to be important in the degassing process, the equilibrium model being used will need to be modified.

C. Numerical Modeling: Homogeneous Media Studies

By using a numerical model, both transient and steady-state conditions can be studied. In addition, the effect of the far-field constant pressure boundary condition can be examined by considering both finite and infinite systems. Under these conditions, the flow geometry has a tremendous effect not only on flow reduction, but on whether a steady state develops at all. In a fractured rock mass the flow geometry is very complicated, as it depends both on the nature of the flow channels within a single fracture plane, and on the connectivity of the network of fracture planes. However, simple models using either linear, cylindrical, or spherical flow geometries provide insight into limiting cases of possible flow geometries in a real rock mass. Linear flow geometry approximates the case in which there are only a few permeable channels within each fracture plane, and fracturing around the borehole is sparse. Spherical flow geometry approximates the opposite case: fluid flows freely throughout fracture planes and fracturing is ubiquitous. Furthermore, the packed-off borehole interval must be short enough to be considered a point source or sink of fluid. Cylindrical flow geometry approximates the intermediate case: either the packed-off borehole interval is long enough to be considered a line source, or fracturing is sparse, or flow is channelized. Figures III.5, III.6, and III.7 show pressure and liquid-saturation profiles for finite and infinite systems for linear, radial, and spherical flow geometry, respectively. For each plot, time is normalized by the liquid-phase diffusion time, which quantifies how long it takes a pressure pulse to propagate a distance through the medium in the absence of a separate gas phase. The difference between finite and infinite systems decreases strikingly as flow dimension increases, because pressure changes are more localized around the borehole. For linear geometry, no steady state develops for an infinite system (Figure III.5, middle row), whereas for radial geometry a quasi-steady state develops (Figure III.6, middle row), and for spherical geometry there is no difference between finite and infinite systems (Figure III.7). Because the pressure decline becomes more localized around the borehole as flow dimension increases, the region in which degassing occurs (where pressure is below the bubble pressure) becomes smaller.

Figures III.8, III.9, and III.10 show q/q_o versus time for linear, radial, and spherical flow geometries. The q/q_o value given by the analytical solution is also shown, as a symbol at the final time. Figure III.8 shows that for linear flow geometry, the finite and infinite medium cases show totally different behavior after the outer boundary is felt (about t/t_{diff} = 3 to 30). For the finite medium, the steady-state normalized flow rates agree reasonably with the analytical solution. The time required to reach steady state increases strongly with gas content, and some oscillation in flow rate is seen before steady-state conditions are reached. For the infinite medium, flow rate declines steadily to zero, with the increased compressibility of a two-phase fluid causing the decline to occur at later times for greater gas content. Thus at any given time, degassing causes a flow increase rather than reduction. For radial geometry (Figure III.9) the difference between finite and infinite media is still apparent, but in both cases greater gas content causes greater flow reduction. For the finite medium, the normalized flow rates at steady state agree reasonably well with the analytical solution. For spherical geometry (Figure III.10) there is no difference between finite and infinite media. Once again, the normalized flow rates at steady state agree reasonably well with the analytical solution. The time required to reach steady state generally increases with gas content, and decreases as flow dimension increases, as shown in Figure III.11.

The integral finite difference method (IFDM) for spatial discretization (Edwards, 1972; Narasimhan and Witherspoon, 1976), which is employed in TOUGH2, can model a variety of flow geometries. With the IFDM, the flow domain is discretized by creating a mesh of (possibly irregularly-shaped) blocks. For the present work, a mesh generator has been developed to create a mesh for a uniform medium with arbitrary flow dimension ranging from n=1 (linear) to n=3 (spherical). This mesh generator was used not only for the calculations illustrated above for n=1, n=2, and n=3, but also to create meshes with non-integral flow dimensions which may be used to represent incompletely connected fracture networks (Barker, 1988). The underlying concept of the mesh generator is that for a flow dimension n and a block of length r, the block volume is proportional to r^n and the block surface area is proportional to r^{n-1}. Thus to create a one-row TOUGH2 mesh one need only specify the desired flow dimension n ($1 \leq n \leq 3$) and a series of block lengths. The mesh generator calculates the appropriate block volumes and surface areas so that the one-row mesh represents flow through an n-dimensional domain. Note that this simple technique only works for uniform media, in which flow is unidirectional (e.g. for n=2 flow is purely radial). Figures III.12 and III.13 show q/q_o versus time for flow dimensions of n=1.4 and n=2.4, respectively. As expected, the variation in q/q_o for n=1.4 is intermediate between that for n=1 and n=2, whereas the variation for n=2.4 is intermediate between n=2 and n=3.

In conclusion, relaxing the assumptions of the analytical solution did not improve the model's prediction of the Stripa SDE results or those of laboratory experiments. However, the numerical solution verified the essential features of the analytical solution. Firstly, if a steady-state value of q/q_o exists (finite media for linear or radial flow geometries, finite or infinite media for spherical flow geometry), it is independent of flow dimension. Secondly, flow reduction increases as gas content increases. The steady-state flow reduction predicted by the numerical simulations generally agrees with the analytical solution, but as the amount of gas present increases, the analytical-solution approximation gets worse.

D. Numerical Modeling: Heterogeneous Media Studies

All the numerical simulations described above considered a homogeneous medium characterized by a single value of permeability. However, the laboratory experiments being conducted with fracture replicas indicate that heterogeneity within the flow domain has an important effect on the magnitude of flow reduction. Therefore, a two-dimensional numerical model of the Dixie Valley fracture replica was created in order to examine the effect of a heterogeneous medium on flow reduction. The fracture replica is about 74 mm on a side and the aperture distribution is given as a 369 by 369 array of aperture values, each representing a 0.02 mm by 0.02 mm square. Using these values directly would result in a model with over 130,000 elements, which would be impractical for numerical simulation. After some study, it was decided to arithmetically average over 9 by 9 blocks of adjacent aperture values to obtain a 41 by 41 array of aperture values, each representing a 0.18 mm by 0.18 mm square. This results in a model with 1681 elements representing the fracture replica (Figure III.14) and an additional 82 elements representing the constant-pressure boundaries. Doing harmonic or geometric averaging rather than arithmetic averaging did not make much difference in the averaged aperture distribution, and using a more finely discretized 123 by 123 array of apertures (averaging over 3 by 3 blocks) did not greatly alter the nature of the heterogeneity. After averaging, the aperture values for each grid element were assigned to one of five values as shown below:

Averaged aperture value for 9 by 9 blocks, microns	Element aperture value, microns
0–50	25
50–100	75
100–150	125
150–200	175
200–250	225

The cubic law was then used to determine the permeability of the element. The characteristic curves were taken from the Van Genuchten [1980] formulation:

$$k_{rl} = \sqrt{\tilde{S}_l}\,[1-(1-\tilde{S}_l^{\,1/\lambda})^{\lambda}]^2 \tag{III.7}$$

$$P_{cap} = P_c[\tilde{S}_l^{\,-1/\lambda} - 1]^{(1-\lambda)} \tag{III.8}$$

$$\tilde{S}_l \equiv (S_l - S_{lr})/(1 - S_{lr} - S_{gr}) \tag{III.9}$$

Capillary pressure strength, P_c, is inversely proportional to element aperture. For the present study $\lambda = 0.5$ and, for simplicity $S_{lr} = S_{gr} = 0$. Gas-phase relative permeability, k_{rg}, was then defined analogously to liquid-phase relative permeability, k_{rl}:

$$k_{rg} = \sqrt{\tilde{S}_g}\,[1-(1-\tilde{S}_g^{\,1/\lambda})^{\lambda}]^2 \tag{III.10}$$

where $\tilde{S}_g \equiv 1 - \tilde{S}_l$. As shown in Figure III.5, this formulation results in strong phase interference and setting residual saturations to zero is a good approximation.

A numerical simulation of flow from the right to the left of the model shown in Figure III.14 yielded the steady-state pressure distribution shown in Figure III.16. The pressure is held fixed at 500 kPa on the right side of the flow domain and 100 kPa on the left side; the top and bottom boundaries are closed. This flow geometry matches that used in the laboratory, but the boundary conditions are adjusted to bracket the bubble pressure for nitrogen, rather than the carbon dioxide values used in the lab. As expected, variations in the aperture distribution are manifested in the pressure distribution, such as the greater variability in aperture in the left half of the model resulting in greater curvature in the pressure contours. Figure III.16 shows the steady-state gas saturation distribution. As expected, there is a close correspondence between pressure and saturation distributions, with two-phase conditions occurring only below the bubble pressure. Figure III.17 shows the variation of q and q_0 as a function of time. Just as in the simulations of homogeneous media, when degassing occurs there is some oscillation before steady state is reached. The final normalized flow value is slightly larger than the analytical solution, and not nearly as small as laboratory values using the Dixie Valley fracture replica, indicating that simply adding heterogeneity to the model is insufficient to produce a significantly greater flow reduction.

The steady-state value of q_0 shown in Figure III.17 may be used in Equations II.1 and II.2 to determine a value of $b = 32$ µm for the effective hydraulic aperture of the fracture model.

This value compares reasonably to the arithmetic average of the fracture replica apertures determined by light attenuation (45 μm), but is much larger than the hydraulic aperture value obtained in the laboratory experiments (9.4 μm). Therefore, in an attempt to more closely match the laboratory conditions, a second model was developed in which 25 μm was subtracted from all apertures to approximately account for loading on the fracture replica. Additionally, the small-aperture variability was better resolved by assigning apertures between 0 and 50 μm into four levels, rather than combining them into one level as before. Aperture values were assigned as follows:

Averaged aperture value for 9 by 9 blocks, microns	Element aperture value, microns
0–25	0 (an asperity)
25–30	2.5
30–40	10
40–50	20
50–100	50
100–150	100
150–200	150
200–250	200

Figure III.19 shows the variation of q and q_0 with time for both the new model with asperities and the original model. The steady-state value of q_0 for the model with asperities yields a value of $b = 13$ μm for effective hydraulic aperture, much closer to the laboratory value than the original model. Although the addition of asperities decreases flow whether or not gas is present, the steady-state normalized flow q/q_o is unchanged from the original value. Steady-state pressure contours are shown in Figure III.20. As in the original model, there is a strong correspondence between the aperture distribution and the pressure contours, illustrating the added flow-path tortuosity caused by asperities. Figure III.20 also shows the steady-state gas saturation. As expected, gas appears only for pressures below the bubble pressure. Unlike the original model, the gas saturation distribution shown in Figure III.20 compares favorably with the experimental gas distribution shown in Figure II.A.8, indicating that some features of the actual fracture replica are being represented correctly in the numerical model. To better understand the flow field across the fracture replica, it is instructive to plot the effective permeability (or mobility), which is the product of absolute permeability (proportional to aperture cubed) and relative permeability (a non-linear function of liquid saturation). Figure III.21 shows the distribution of mobility on a relative scale from 0 to 100. It indicates that there are three or four prominent flow paths along which the minimum mobility is in the range from 10 to 30 (yellow or orange on Figure III.21). The existence of only a few prominent flow paths is confirmed by Figure III.22, which shows the variation of outflow across the fracture replica for both no-gas and with-gas conditions. It is also of interest to note that for the most part as gas is added to the system, flow decreases in large-flow elements, while in small-flow elements flow increases. This phenomenon is a consequence of the greater strength of capillary pressure in the smaller aperture elements, which drives the gas phase into the large-aperture regions (where it decreases liquid flow) and the liquid phase into the small-aperture regions (where it enhances liquid flow). The findings of Figures III.21 and III.22 illustrate the need for a careful representation of fracture aperture distribution, and suggest that it might be beneficial to use a model in which each element has an individual aperture value, rather than using only eight different values as is currently done. Future studies will consider the effect of capillary pressure in heterogeneous media which may differ from its effect in homogeneous media, discussed earlier.

Several other variations on the numerical model of flow through the fracture replica were made, but none predicted a greater flow reduction than given by the analytical solution (see Figure III.23). These variations included using smaller gas content, a uniform aperture distribution, a non-zero irreducible gas saturation, modeling flow in the opposite direction through the fracture replica, and varying the parameters of the characteristic curves. A more systematic study of the effect of characteristic curves will be conducted in the future.

E. Conclusions from Modeling Studies and Plans for Future Modeling Work

Relaxing some of the assumptions required for the simple analytical solution of flow reduction due to degassing necessitated a numerical model to simulate flow and degassing. In particular, the model was extended from steady-state to transient conditions, from finite to infinite media, from linear to radial, spherical, and non-integral flow geometries, and from a homogeneous medium to a heterogeneous medium. None of the extensions to the conceptual model has significantly increased the flow reduction due to degassing from that predicted by the original analytical solution. Hence all the modeling studies significantly under-predict the effect of degassing on fluid flow measured in the laboratory and at the Stripa SDE. However, we have only modeled one heterogeneous case. The Stripa fracture will be modeled to see if the relative differences in flow reduction due to the different fracture geometries observed in the laboratory experiments are reproduced in the model. The next assumption to be investigated is that of equilibrium between degassing and redissolution, which will be carried out by adding non-equilibrium effects to TOUGH2. Three possible approaches are being considered. In order of increasing complexity (and rigor) they are: to consider degassing only, with no redissolution possible; to use a hysteretic form of Henry's law which makes degassing occur more readily than dissolution; and to use kinetic rate equations for both degassing and dissolution. Additionally, as other fracture replicas and flow geometries are used in laboratory studies, they will be modeled as well.

Part IV. Summary and Conclusions

Figure IV.1 provides an overview of the LBL work on two-phase flow and excavation effects to date. We began with the observation at the Stripa SDE that suggested degassing caused a large flow reduction (a factor of nine). This initiated two branches of work: 1) laboratory and field studies which attempted to replicate the Stripa SDE results under better-controlled conditions; and 2) modeling studies to attempt to understand and predict the effects of degassing. Laboratory studies investigating linear flow through transparent fracture replicas did indicate significant flow reductions, and suggested that fracture geometry has a critical effect on the magnitude of flow reduction. Preliminary field experiments at HRL will be conducted in the next year. Increasingly sophisticated numerical models have not yet predicted the large flow reductions due to degassing, but some features of the laboratory experiments have been reproduced. Understanding degassing phenomena in particular and two-phase flow phenomena in general is important because we need to develop a fundamental understanding of flow in fractures and fracture networks, in order to successfully model conditions around a nuclear waste repository, whose long time and large space scales preclude conclusive field experiments.

Acknowledgement

This work was carried out under U.S. Department of Energy Contract No. DE-AC03-76SF00098, for the Director, Office of Civilian Radioactive Waste Management, Office of External Relations, administered by the Nevada Operations Office and under the Swedish Nuclear Fuel and Waste Management Company (SKB) Contract NO. 268070. Numerical computations were supported by the Director, Office of Energy Research, Office of Basic Energy Sciences, Engineering and Geosciences Division, U.S. Department of Energy. We would like to thank Peter Persoff for the use of his experimental apparatus.

Part V. References

Adamson, A. W., 1982. Physical Chemistry of Surfaces. John Wiley & Sons, Inc., New York, 664 pp.

Andres, J.N., Hussain, N. and Youngman, M.J., 1989. Atmospheric and radiogenic gases in groundwaters from the Stripa Granite, Geochemica et Cosmochemica Acta, 53, 1831-1841.

Barker, J.A., 1988. A generalized radial flow model for hydraulic tests in fractured rock. Water Resources Res., 24, 1796-1804.

Cox, B. L. and J. S. Y. Wang, 1993. Single fracture aperture patterns: characterization by slit-island fractal analysis. Proceedings of the Fourth International High-Level Radioactive Waste Management Conference, Las Vegas, Nevada, April 26-30.

Davies, P., J. C. S. Long and P. Zuidema, 1993. Two-phase flow in fractured rock. Proceedings of the Two-Phase Flow in Fractured Rock Workshop, Berkeley, CA November 3-5, 1993. Lawrence Berkeley Laboratory report LBL-35387, UC-400, 51 pp.

Edwards, A.L., 1972. TRUMP: A computer program for transient and steady state temperature distributions in multidimensional systems, National Technical Information Service, National Bureau of Standards, Springfield, VA.

Firoozabadi, A. and D. Kashchiev, 1993. Pressure and volume evolution during gas phase formation in solution gas drive process. SPE 26286.

Glass, R.J. and M.J. Nicholl, in press. Quantitative visualization of entrapped phase dissolution within a horizontal flowing fracture, Geophysical Research Letters, Special Issue, Multiphase Flow in Fractured Rock.

Li, X. and Y. C. Yortsos, 1992. Critical gas saturation: modeling and sensitivity studies. SPE paper 26662.

Narasimhan, T.N. and P.A.Witherspoon, 1976. An integrated finite difference method for analyzing fluid flow in porous media, Water Resources Research, 12 (1), 57-64.

Nicholl, M. J., R. J. Glass, and S. W. Wheatcraft, 1994. Gravity-driven infiltration flow instability in non-horizontal unsaturated fractures. Water Resources Res., 30 (9), 2533-2546.

Olsson, O., ed, 1992. Site characterization and validation - final report, Stripa Project Technical Report 92-22, Swedish Nuclear Fueld and Waste Management Co., Stockholm, Sweden, 364 pp.

Parlar, M. and Y. C. Yortsos, 1989. Bubble growth in porous media: I. Low supersaturations. SPE paper 19697, Annual Fall Meeting of the Society of Petroleum Engineers, San Antonio, TX (October, 1989).

Persoff, P. and Pruess, K., 1993. Flow visualization and relative permeability measurements in rough-walled fractures. Proceedings of the Fourth International High-Level Radioactive Waste Management Conference, Las Vegas, Nevada, April 26-30.

Persoff, P., K. Pruess and L. Myer, 1991. Two-phase flow visualization and relative permeability measurement in transparent replicas of rough-walled rock fractures. Presented at the 16th Workshop on Geothermal Reservoir Engineering, Stanford, California, January 23-25, LBL-30161.

Pruess, K., 1991. TOUGH user's guide. Rep. LBL-20700, Lawrence Berkeley Lab., Berkeley, CA.

Pruess, K., 1987. TOUGH2 - A general-purpose numerical simulator for multiphase fluid and heat flow. Rep. LBL-29400, Lawrence Berkeley Lab., Berkeley, CA.

van Genuehten, M.T., 1980. A closed-form equation for predicting the hydraulic conductivity of unsaturated soils. Soil Sci. Soc. Am. J., 44, 892-898.

Vomvoris, S., and B. Frieg, eds., 1991. Grimsel Test Site, Overview of Nagra field and modeling activities in the Ventilation Drift (1988-1990). Nagra Technical Report NTB 91-34.

Nomenclature

b	effective hydraulic aperture
dh/dl	hydraulic gradient
g	acceleration gravity
H	Henry's Law Constant
h	plate separation or aperture height
k	permeability
k_r	relative permeability
L	length
L_b	bubble length
P	pressure
$P*$	normalized bubble pressure
P_0	borehole boundary pressure
P_1	far-field boundary presure
P_{CO_2}	partial pressure of CO_2
q	flowrate
q_0	flowrate for liquid phase conditions
S	saturation
V	volume
w	fracture edge width
x	mole fraction, aqueous phase
y	mole fraction, gas phase
λ	van Genuchten parameter
μ	dynamic viscosity
$\overline{\upsilon}$	molar volume
ρ	fluid density
σ	surface tension
θ	contact angle (measured through wetting phase)
a	species
b, B	bubble
c	capillary strength
cap	capillary
g	gas

g,r	gas, irreducible
l	liquid
l,r	liquid, irreducible
T	total

Figure Captions

Figure I.1. Trapped bubble length as a function of restriction size. Bubble lengths less than the plotted value will be trapped by the restriction.

Figure II.A.1. Flowchart for degassing experiments

Figure II.A.2. Aperture maps of fractures

Figure II.A.3. Pressure and flow data for Dixie Valley Ia experiment.

Figure II.A.4. Pressure and flow data for Dixie Valley Ib experiment.

Figure II.A.5. Pressure and flow data for Dixie Valley II experiment.

Figure II.A.6. Pressure and flow data for Stripa experiment.

Figure II.A.7. Summary of experimental results and comparison with SDE.

Figure II.A.8. Comparison of steady-state gas distribution with aperture distribution. Top images are the steady-state gas distribution for DVIb (right) and S-c (left). White regions indicate gas. Flow direction is from right to left. Bottom images are the aperture distributions, aligned with the gas distributions. White indicates apertures greater than 50 μm. The left edge of the Stripa gas saturation image was out of the field of view of the camera.

Figure II.B.1. Progression from blue to green to yellow to red shows the gas solution process in time. Black indicates locations which contained water throughout the experiment and red where the gas phase remained at the end of the experiment.

Figure II.B.2. Relative concentration field for a dye pulse through a fracture with entrapped air present. The water phase is flowing from bottom to top. Entrapped air phase is indicated with white. Relative concentration of dye (0 to 1) is determined using light adsorption theory. Pure water is gray, dyed water is dark.

Figure II.B.3. Composite image of gravity-driven air invasion in a vertical fracture. Images over a two-day period are summed to visualize the zones where air moves upward under gravitational gradient from the bottom edge of the fracture where evaporation occurs. Air phase is denoted by black and water by light gray.

Figure II.B.4. Sequential images showing upward movement of air in a saturated vertical fracture: This enlargement shows the growth of an air finger from an evaporative front in a water (solid blue) saturated fracture. After growing upward as a finger (center) the invading air structure breaks up and moves as buoyant bubbles until trapped by capillary forces. The region shown here is an enlargement of the area boxed in red on Figure II.B.3.

Figure III.1. Top frame: conceptual model of flow reduction due to degassing for steady-state flow through a one-dimensional homogeneous medium with pressure held fixed at either end. Bottom frame: normalized flow versus normalized gas content for the analytical solution and the Stripa SDE result.

Figure III.2. TOUGH2 calculation for a total gas volume of 5.5%.

Figure III.3. TOUGH2 calculations for a range of λ values.

Figure III.4. TOUGH2 calculations for a case including capillary pressure.

Figure III.5. Simulated pressure (solid lines) and liquid saturation (dashed lines) profiles for linear flow geometry (n=1), finite and infinite media, with and without gas.

Figure III.6. Simulated pressure (solid lines) and liquid saturation (dashed lines) profiles for radial flow geometry (n=2), finite and infinite media, with and without gas.

Figure III.7. Simulated pressure (solid lines) and liquid saturation (dashed lines) profiles for spherical flow geometry (n=3), finite and infinite media, with and without gas.

Figure III.8. Normalized flow (flow under degassing conditions divided by flow with no gas present) as a function of normalized time for linear flow geometry (n=1), finite and infinite media, and various gas contents.

Figure III.9. Normalized flow as a function of normalized time for radial flow geometry (n=2), finite and infinite media, and various gas contents.

Figure III.10. Normalized flow as a function of normalized time for spherical flow geometry (n=3), finite and infinite media, and various gas contents.

Figure III.11. The time required to reach steady state (upper curve of each pair) and 95% of steady state (lower curve of each pair) for various flow geometries and gas contents.

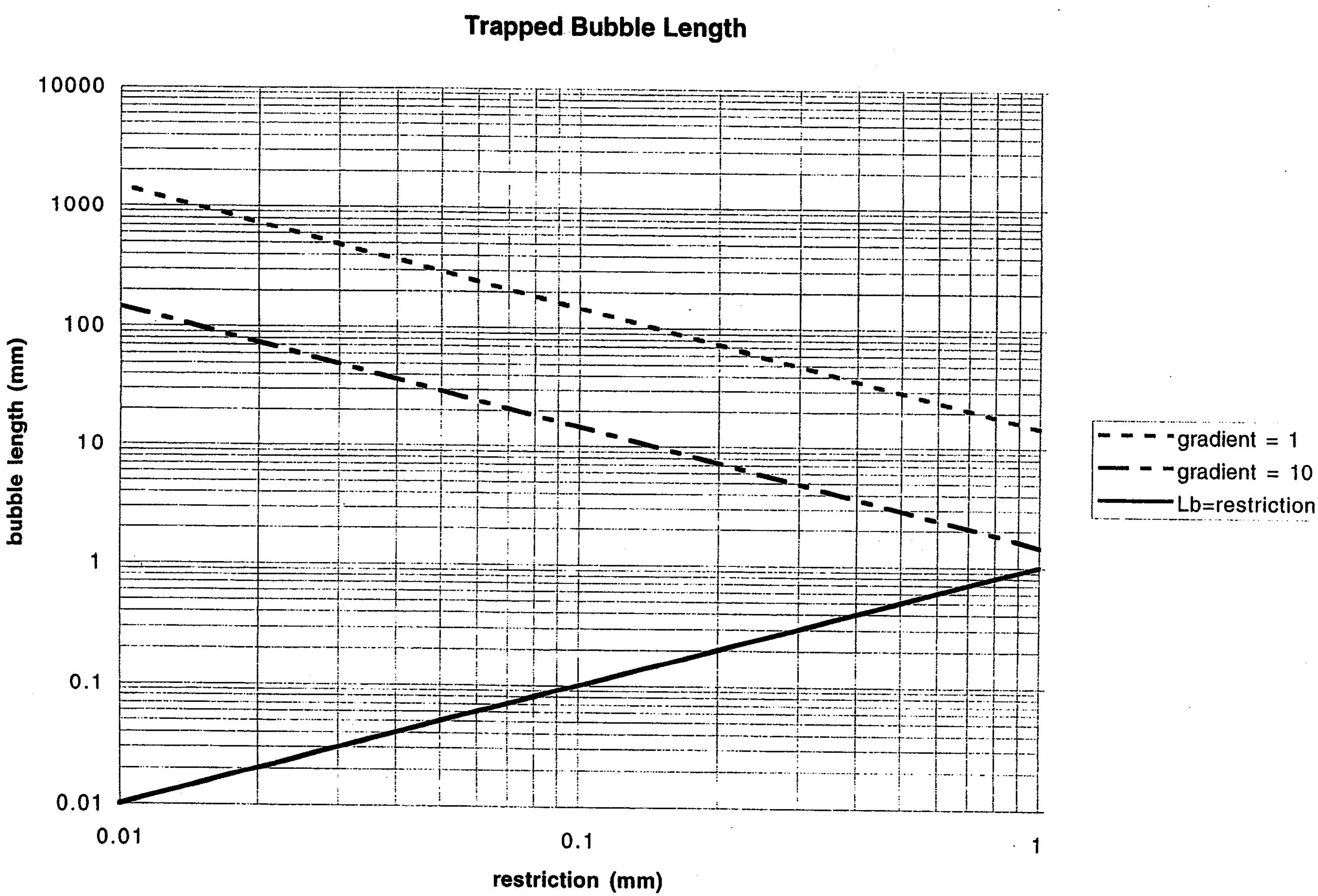
Trapped Bubble Length
10000
1000
100
10
1
0.1
0.01
bubble length (mm)
0.01
0.1
1
restriction (mm)
gradient = 1
gradient = 10
Lb=restriction

Figure I.1

Fracture Assembly

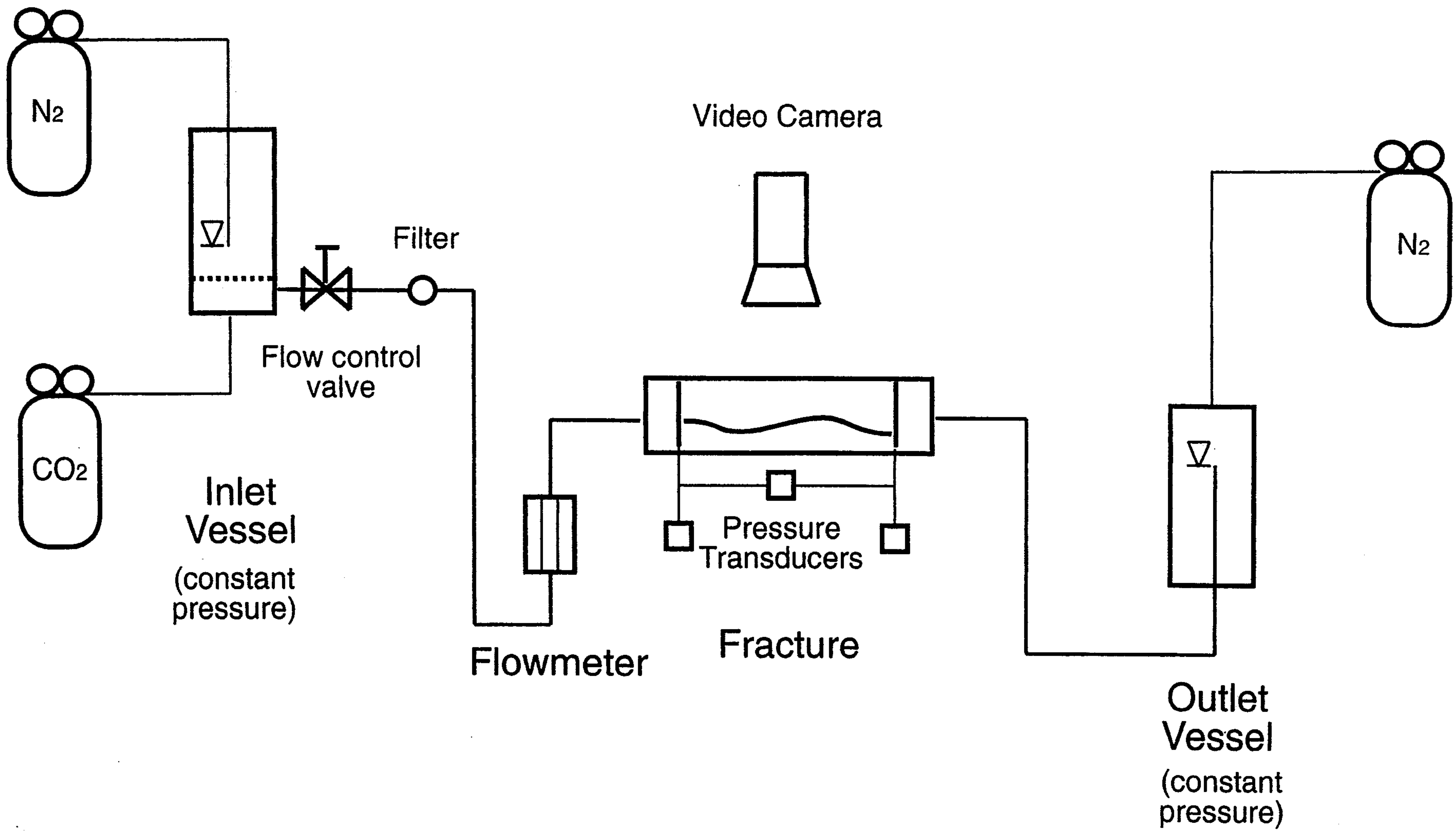

Figure II.A.1

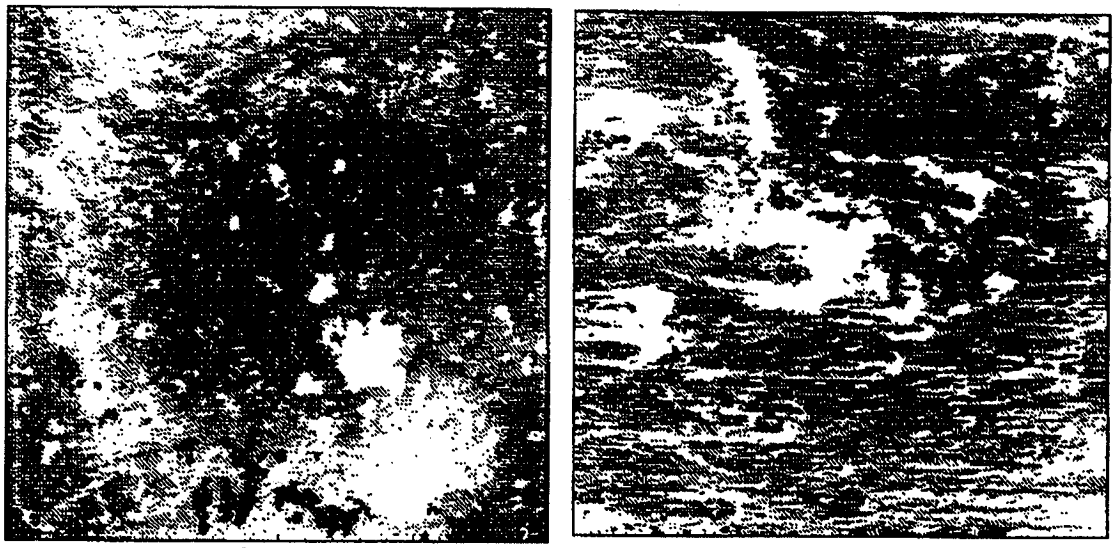

(a) (b)

Figure II.A.2. Aperture maps of fractures used in the laboratory experiments. White areas represent apertures greater than 50 μm, black areas are less than 50 μm. Flow direction is from right to left.

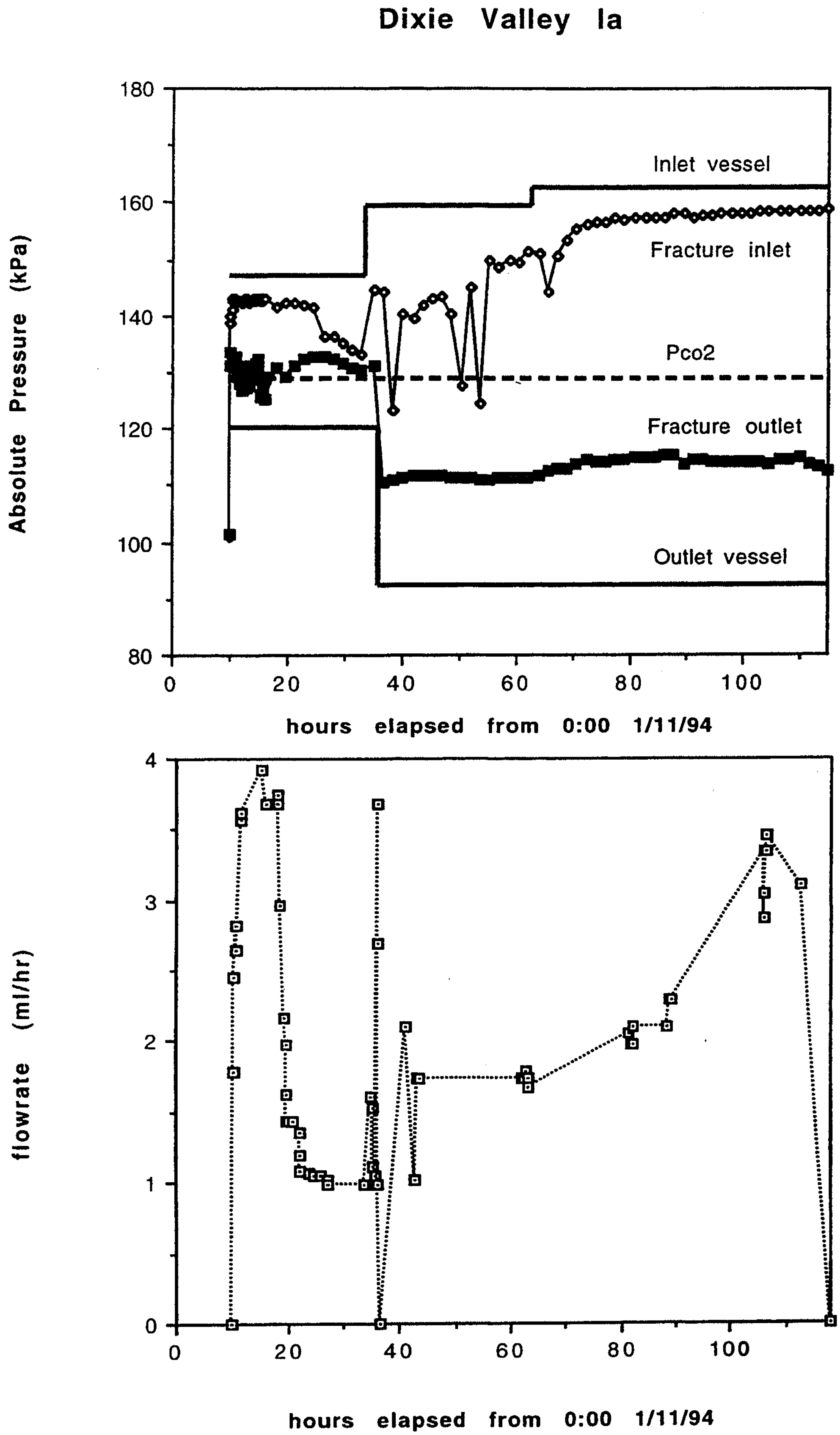

Dixie Valley Ia
Absolute Pressure (kPa)
180
160
140
120
100
80
Inlet vessel
Fracture inlet
Pco2
Fracture outlet
Outlet vessel
0
20
40
60
80
100
hours elapsed from 0:00 1/11/94
flowrate (ml/hr)
4
3
2
1
0
0
20
40
60
80
100
hours elapsed from 0:00 1/11/94

Figure II.A.3

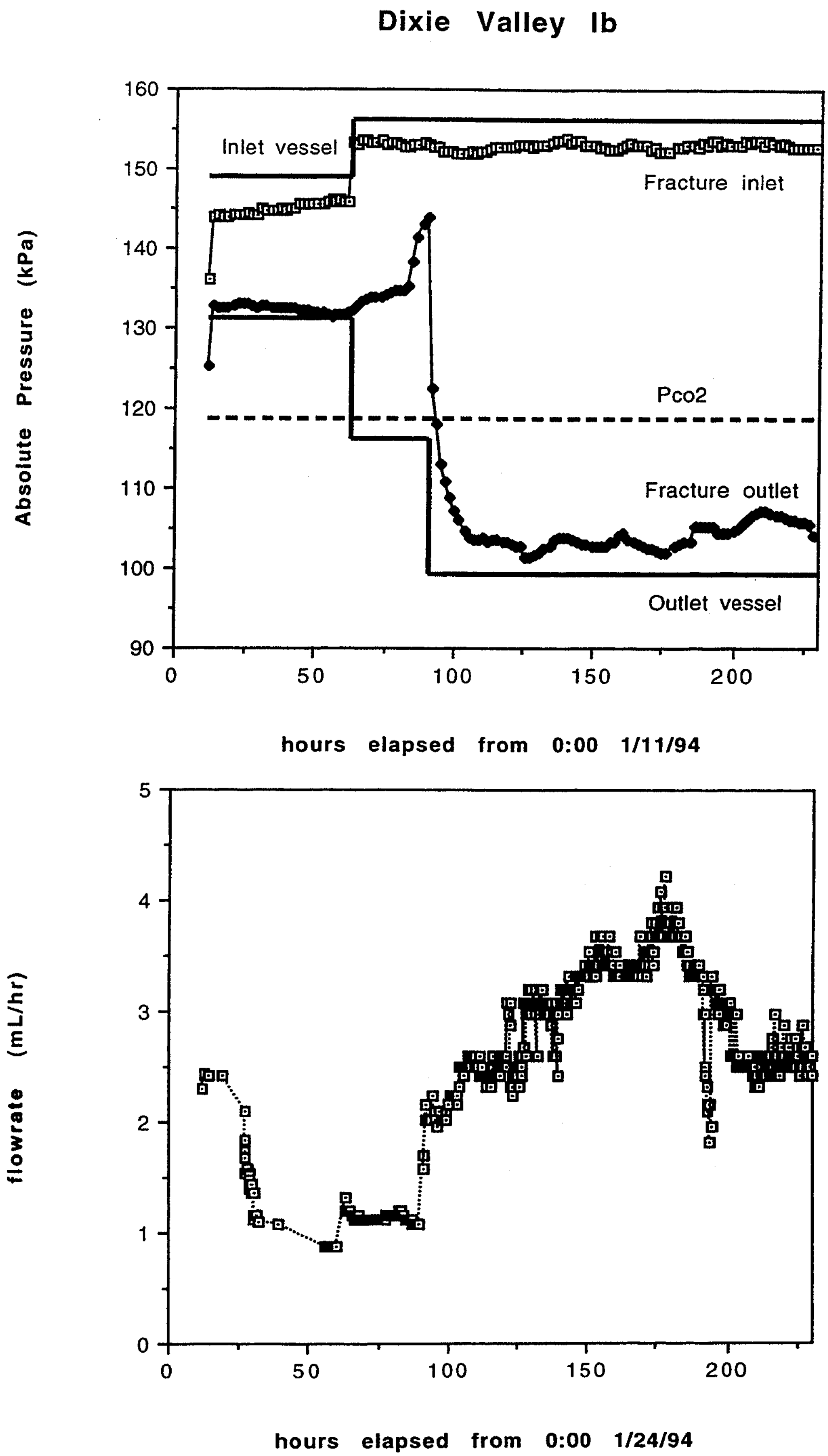
Dixie Valley Ib
Absolute Pressure (kPa)
160
150
140
130
120
110
100
90
0
50
100
150
200
Inlet vessel
Fracture inlet
Pco2
Fracture outlet
Outlet vessel
hours elapsed from 0:00 1/11/94
flowrate (mL/hr)
5
4
3
2
1
0
0
50
100
150
200
hours elapsed from 0:00 1/24/94

Figure II.A.4

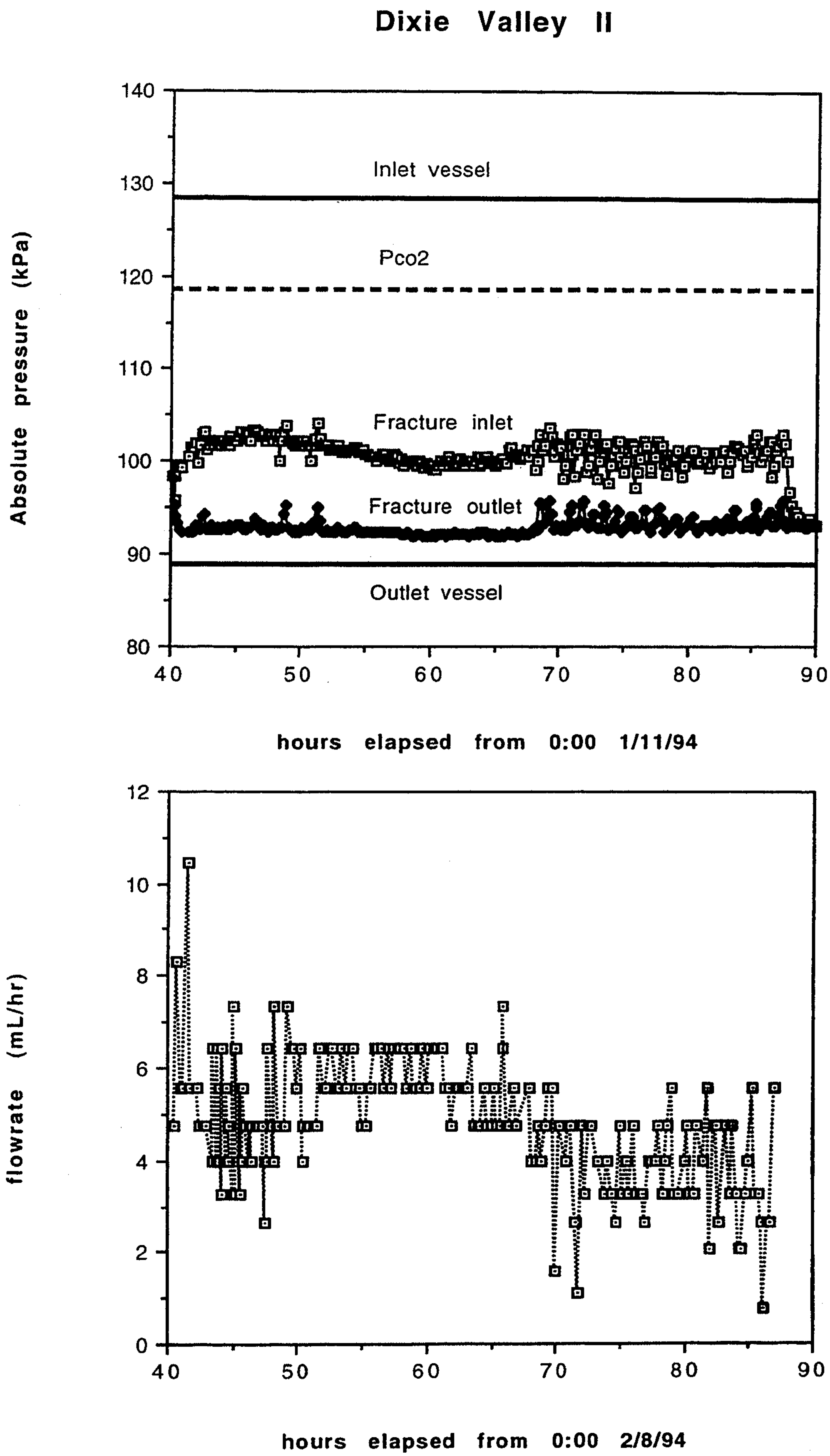

Dixie Valley II
Absolute pressure (kPa)
140
130
120
110
100
90
80
Inlet vessel
Pco2
Fracture inlet
Fracture outlet
Outlet vessel
40
50
60
70
80
90
hours elapsed from 0:00 1/11/94
flowrate (mL/hr)
12
10
8
6
4
2
0
40
50
60
70
80
90
hours elapsed from 0:00 2/8/94

Figure II.A.5

Stripa a, b and c

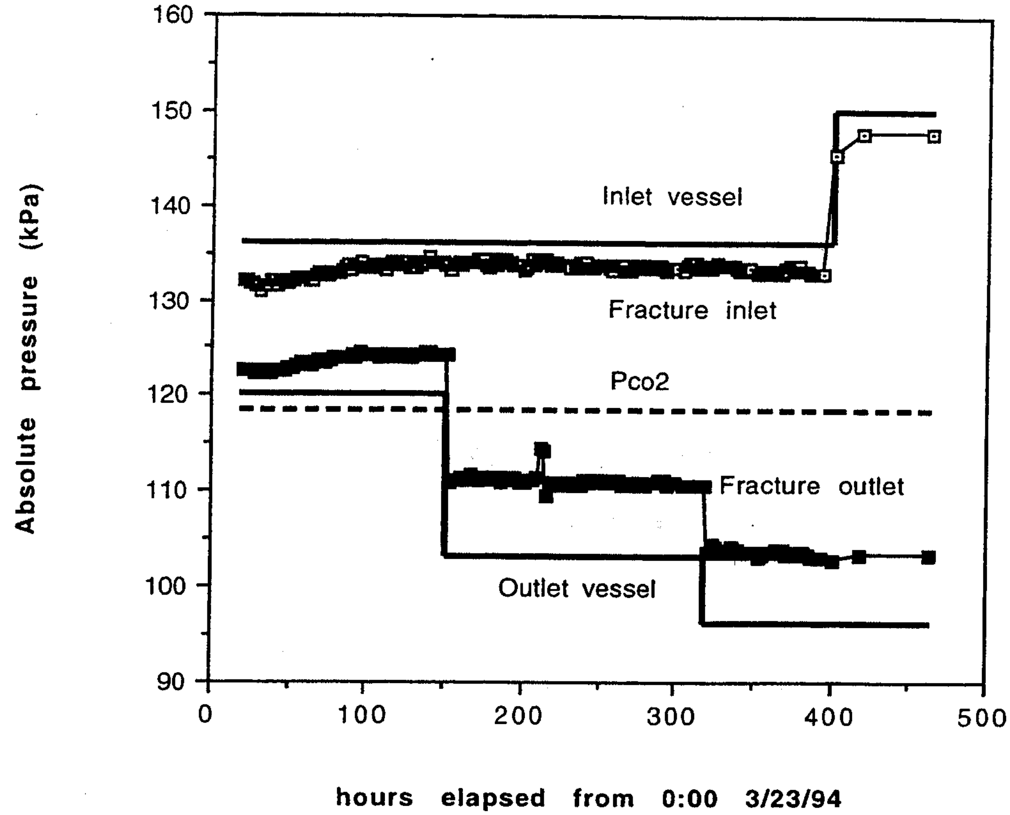

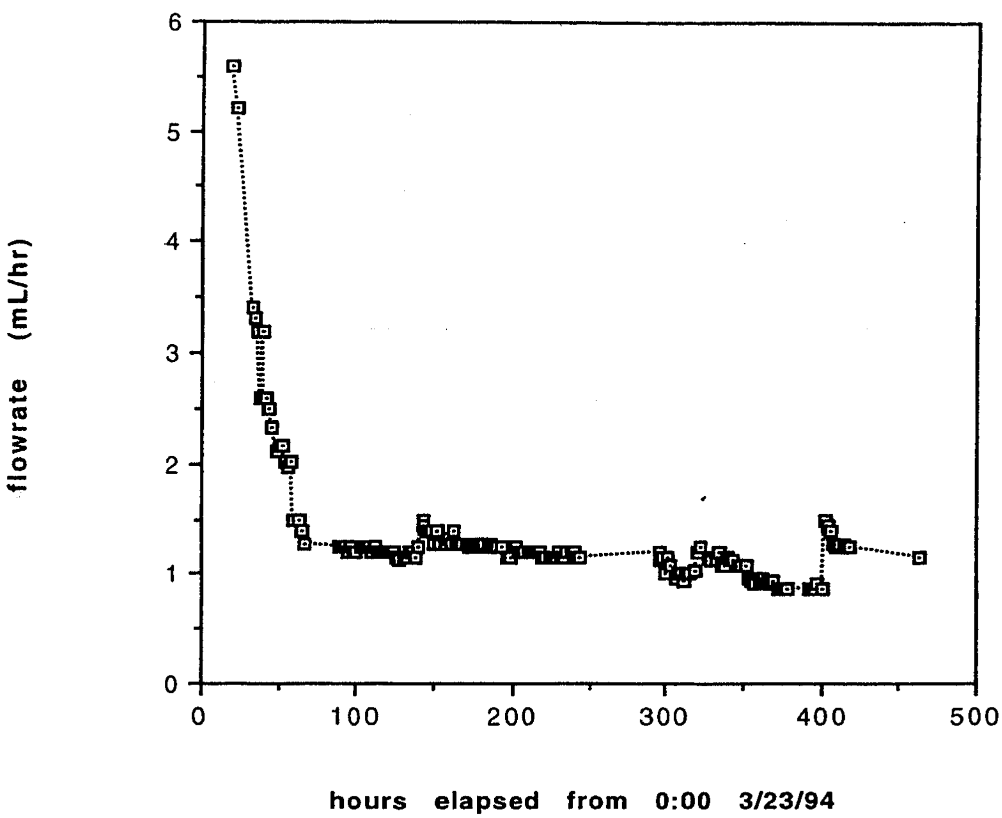

Figure II.A.6

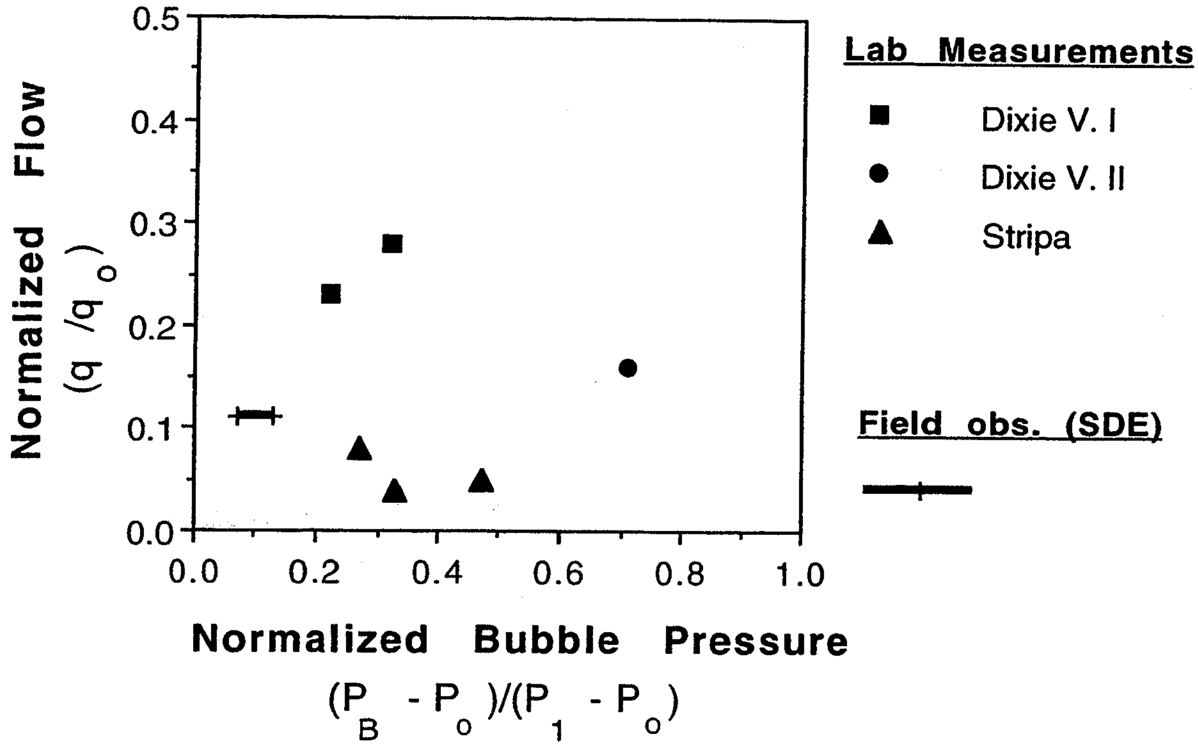

0.5
0.4
0.3
0.2
0.1
0.0
0.0
0.2
0.4
0.6
0.8
1.0
Normalized Flow
(q /q o)
Normalized Bubble Pressure
(P B - P o)/(P 1 - P o)
Lab Measurements
Dixie V. I
Dixie V. II
Stripa
Field obs. (SDE)

Figure II.A.7

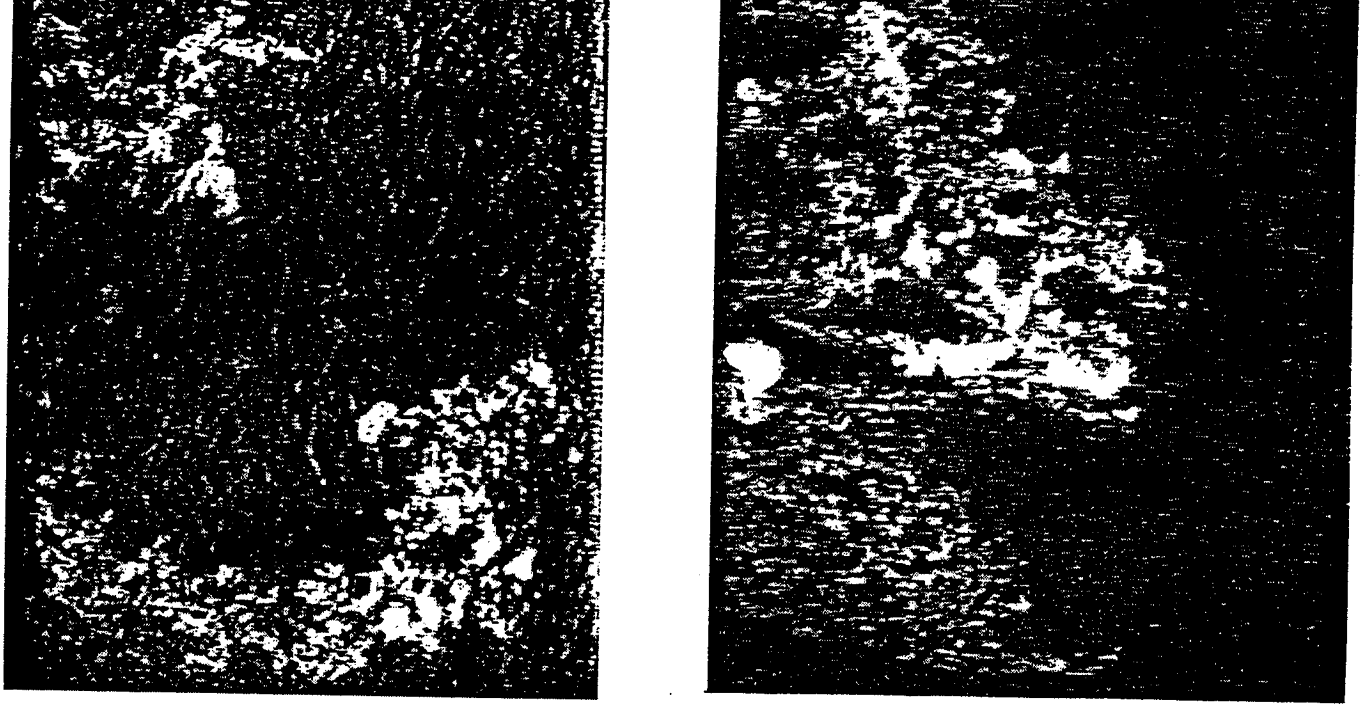

a. Steady State Gas Distribution
(white = gas)

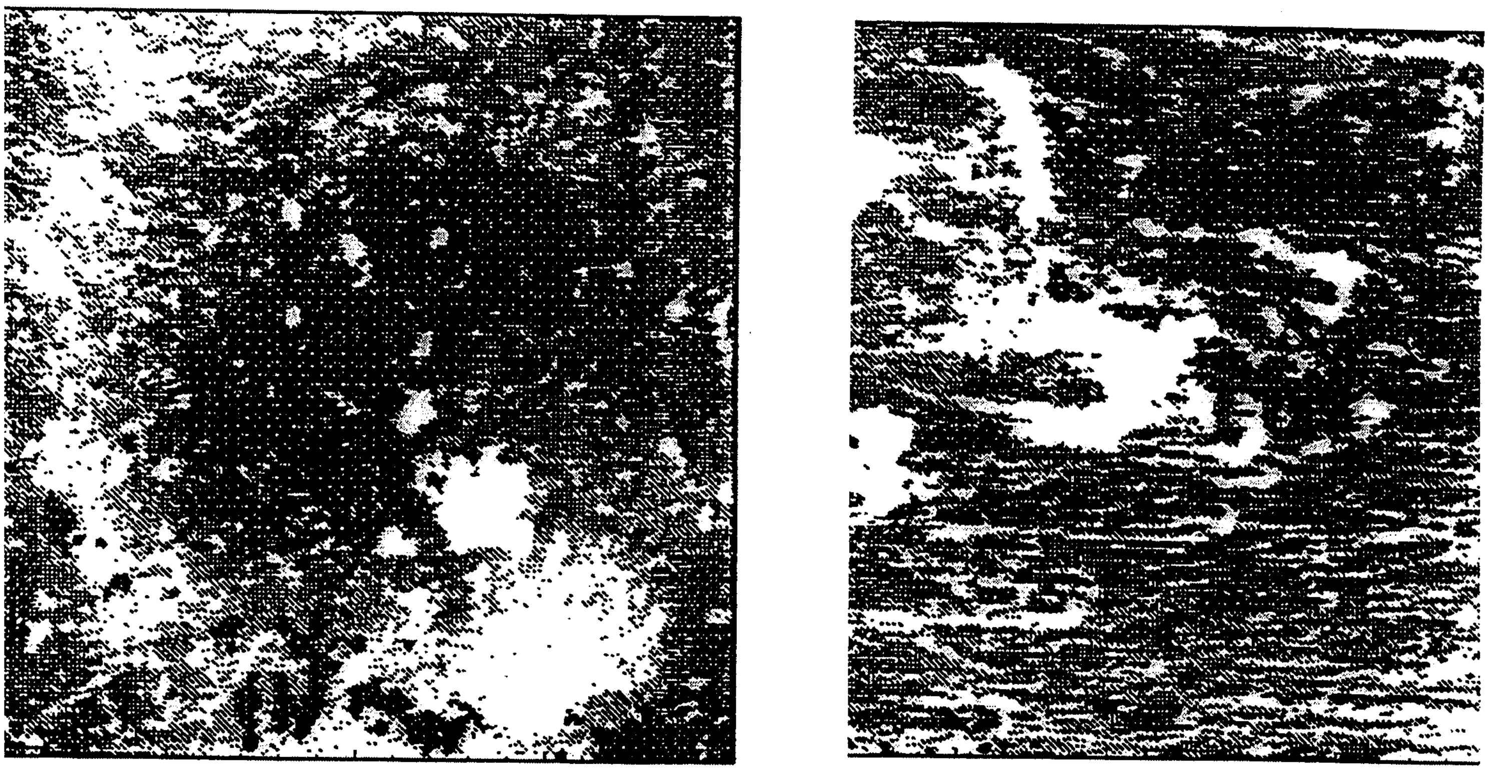

b. Aperture Distribution
(white= > 50 um)

Stripa

Figure II.A.8

Dixie Valley

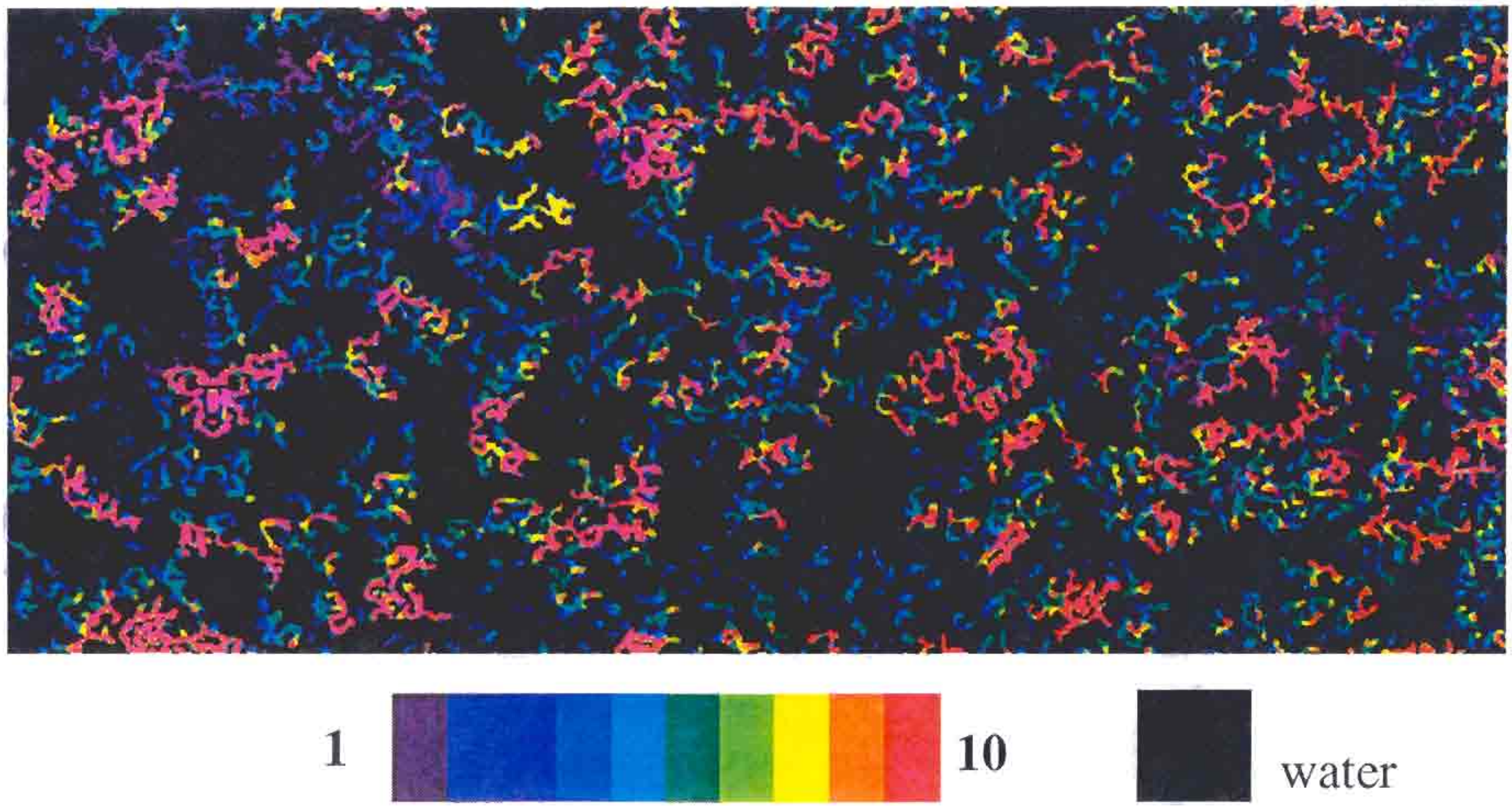

Figure II.B.1: **Composite image of dissolution order:** This image was made by compiling images collected at each of the 9 measurements. Black indicates that the region was initially saturated with water, any other color indicates that the region was air filled at the onset of dissolution. Red areas remained saturated with air throughout the course of dissolution. Purple regions were the first to fill with water, dark blue the second, and so on.

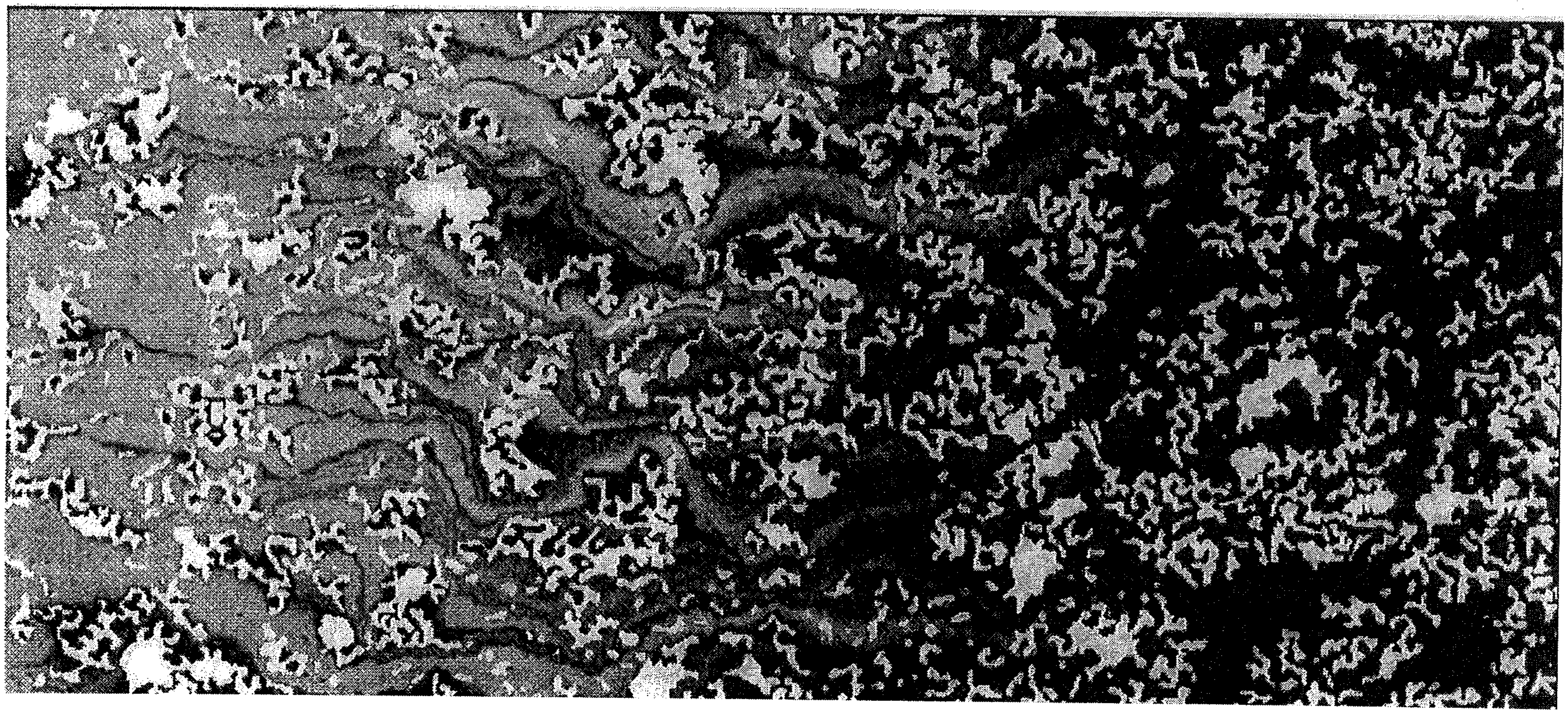

Figure II.B.2: **Flow path visualization during dissolution:** Dyed water in the analog fracture (dark regions) is invaded by pure water (gray) to visualize flow processes channeling induced by the structure of the entrapped air phase (white).

Figure II.B.3: **Composite image of bouyant air invasion into a vertical analog fracture:** As seen in Figure C-1 air invaded the fracture as discrete bouyant bubbles. As a result, indivdual images provide little information on air pathways through the system. This composite image was created by summing the changes in phase occupancy for all images collected during this experiment. The paths taken by the bouyant air bubbles are depicted in black, and the zones that remained water saturated as speckled gray. The red box outlines the region enlarged for Figure C-1.

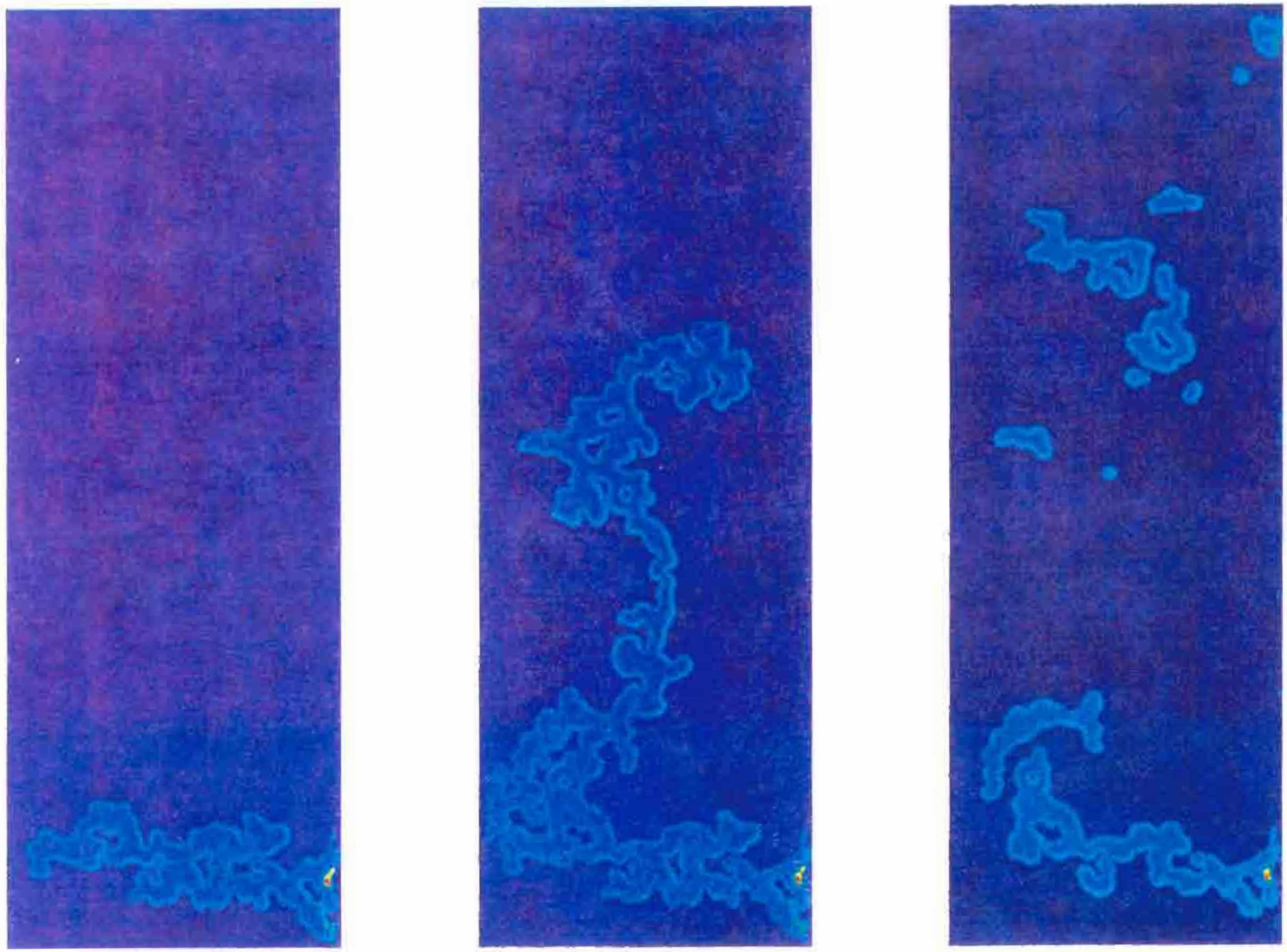

Figure II.B.4: **Sequential images showing upward movement of air in a saturated vertical fracture:** This enlargement shows the growth of an air finger from an evaporative front in a water (solid blue) saturated fracture. After growing upward as a finger (center) the the invading air structure breaks up and moves as bouyant bubbles until trapped by capillary forces. The region shown here is an enlargement of the area boxed in red on Figure C-2.

Simple Analytical Solution

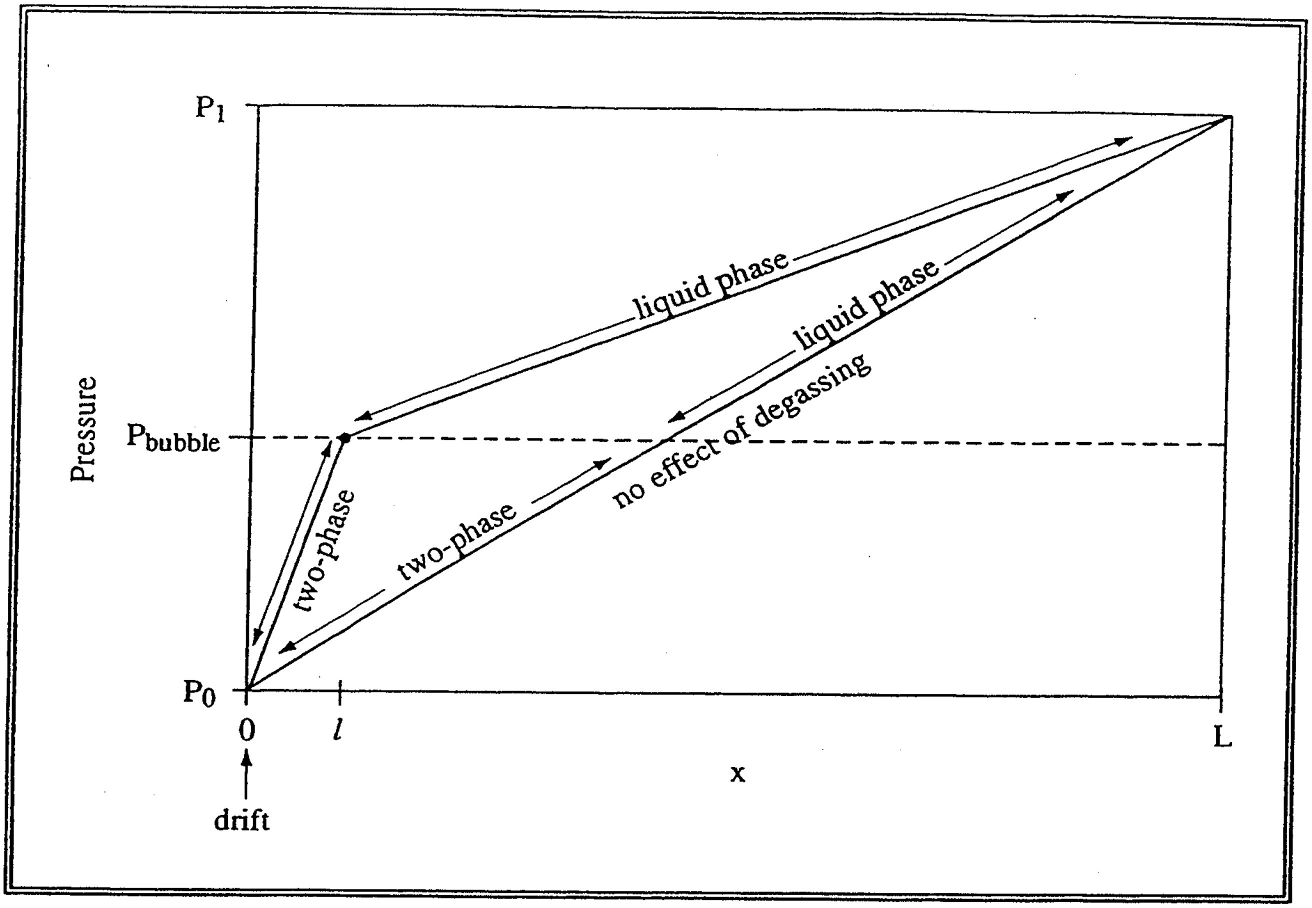

ESD-9311-0009

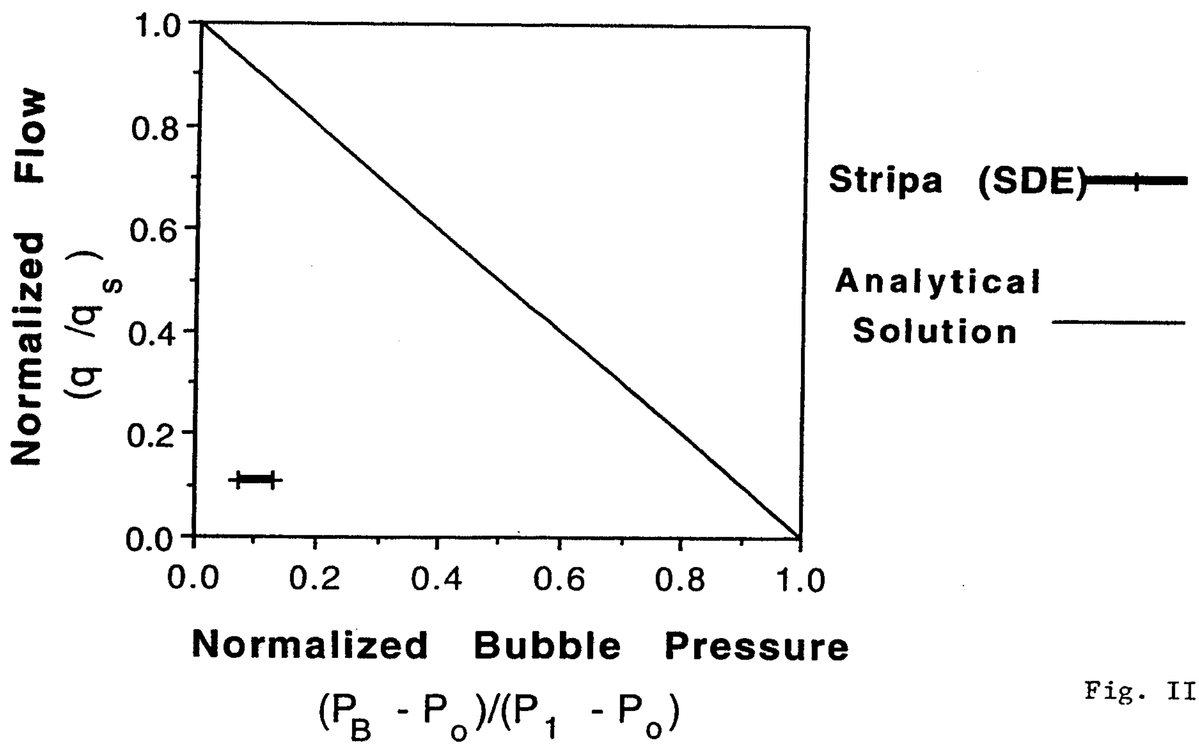

Fig. III.1

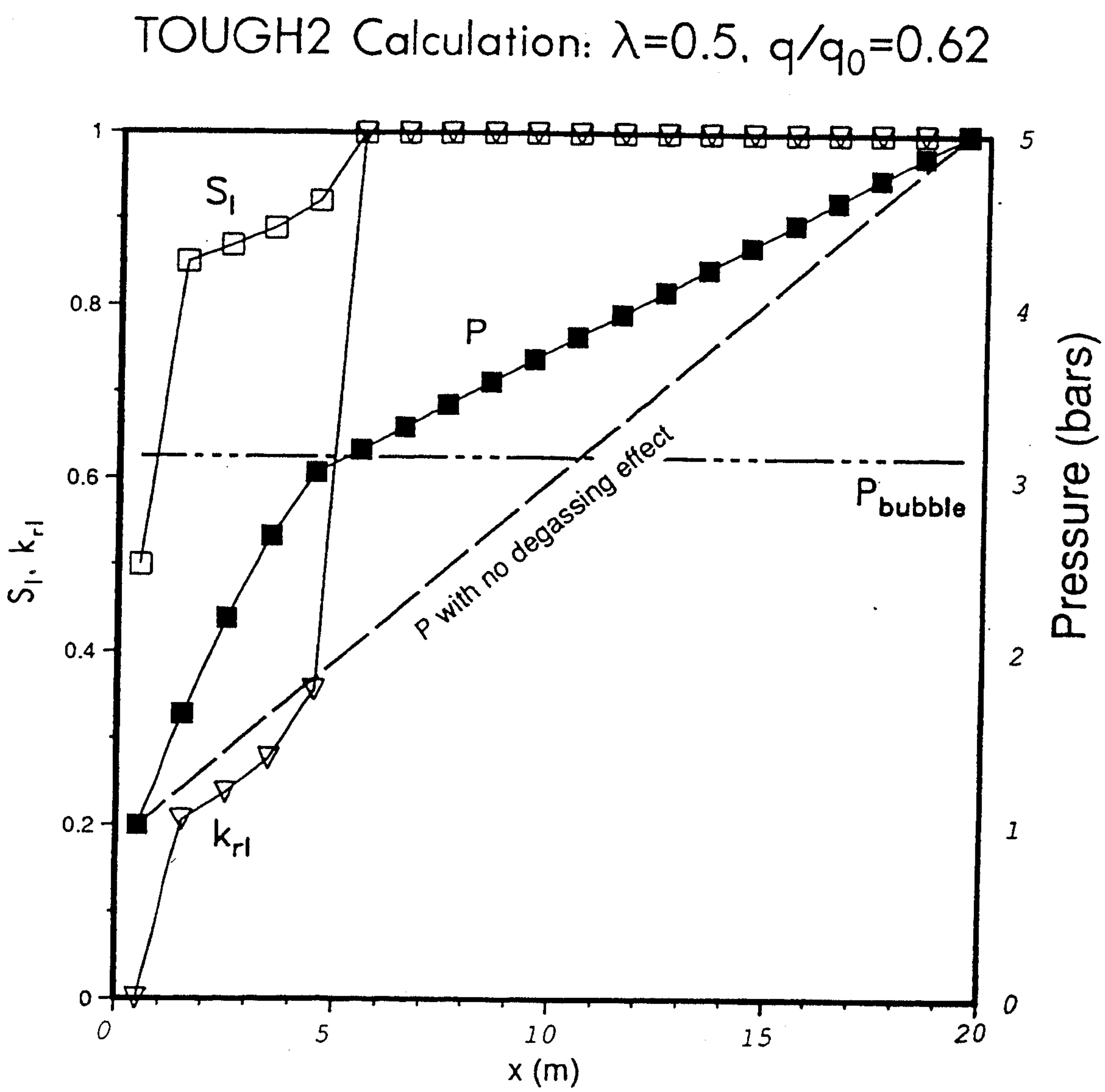

Figure III.2: TOUGH2 calculation for a gas volume percent of 5.5%.

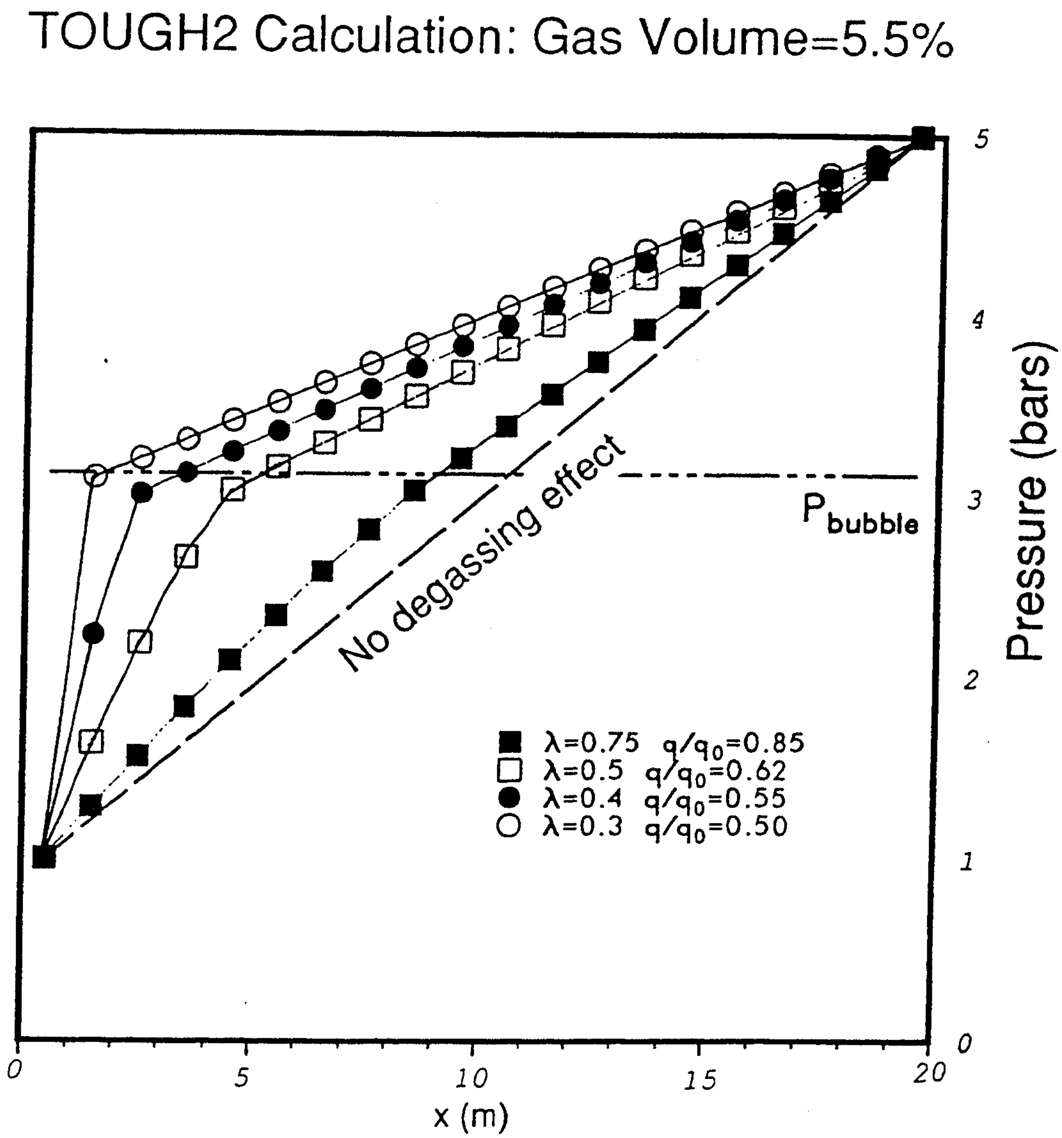

Figure III.3: TOUGH2 calculations for a range of λ values.

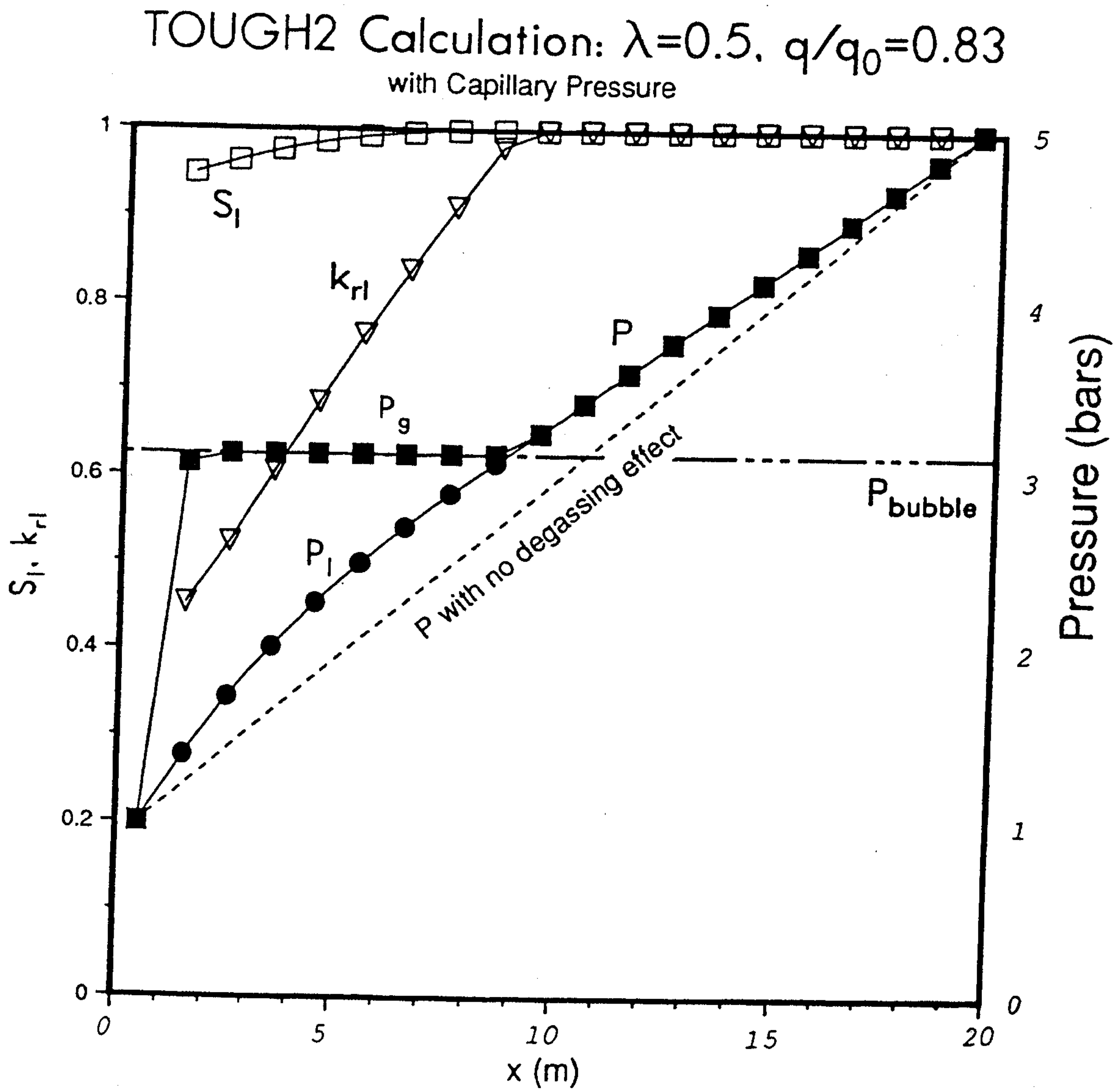

Figure III.4: TOUGH2 calculation for a case including capillary pressure.

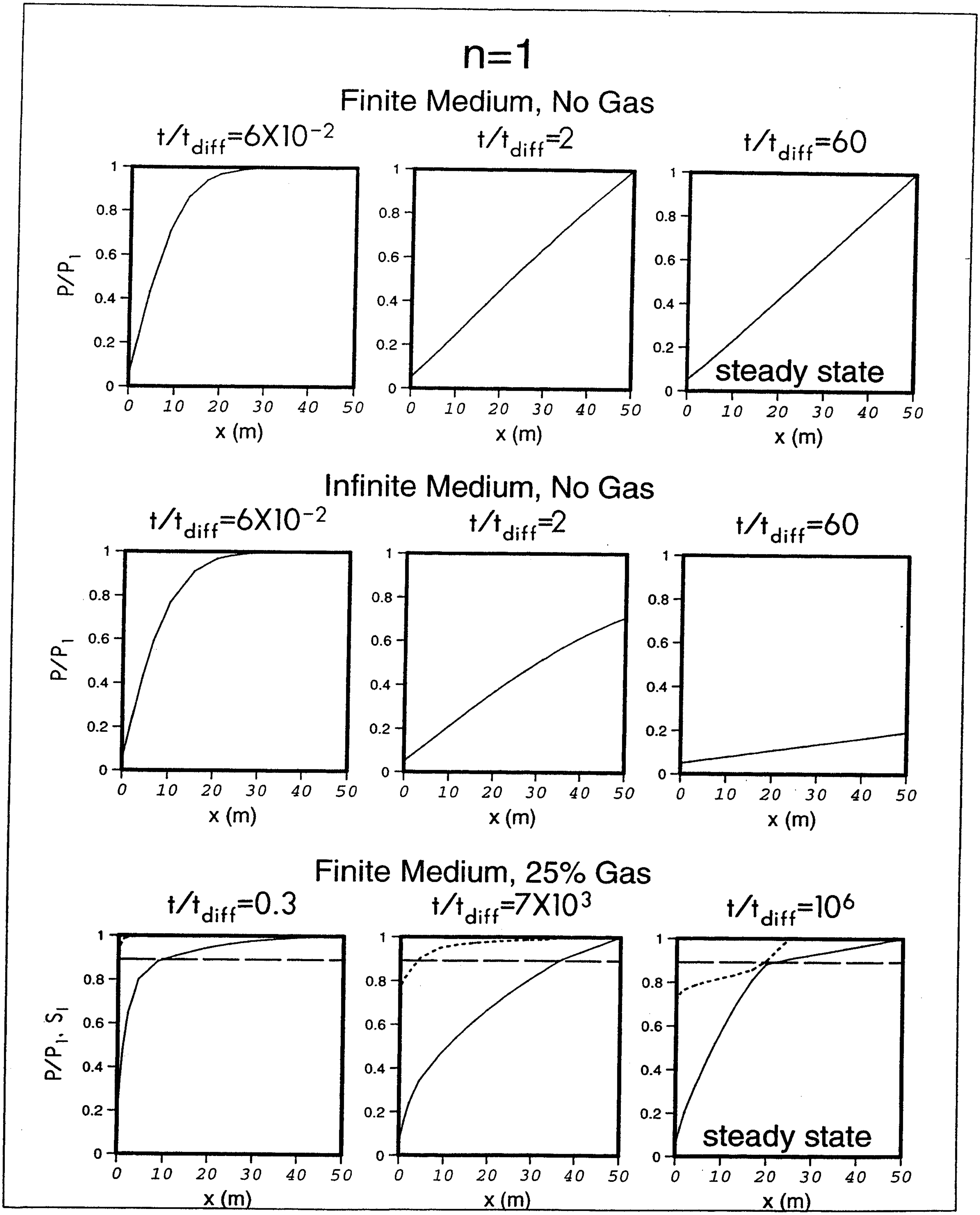
n=1
Finite Medium, No Gas
t/t_diff=6X10^-2
t/t_diff=2
t/t_diff=60
steady state
P/P_l
x (m)
Infinite Medium, No Gas
t/t_diff=6X10^-2
t/t_diff=2
t/t_diff=60
Finite Medium, 25% Gas
t/t_diff=0.3
t/t_diff=7X10^3
t/t_diff=10^6
P/P_l, S_l
steady state

Figure III.5

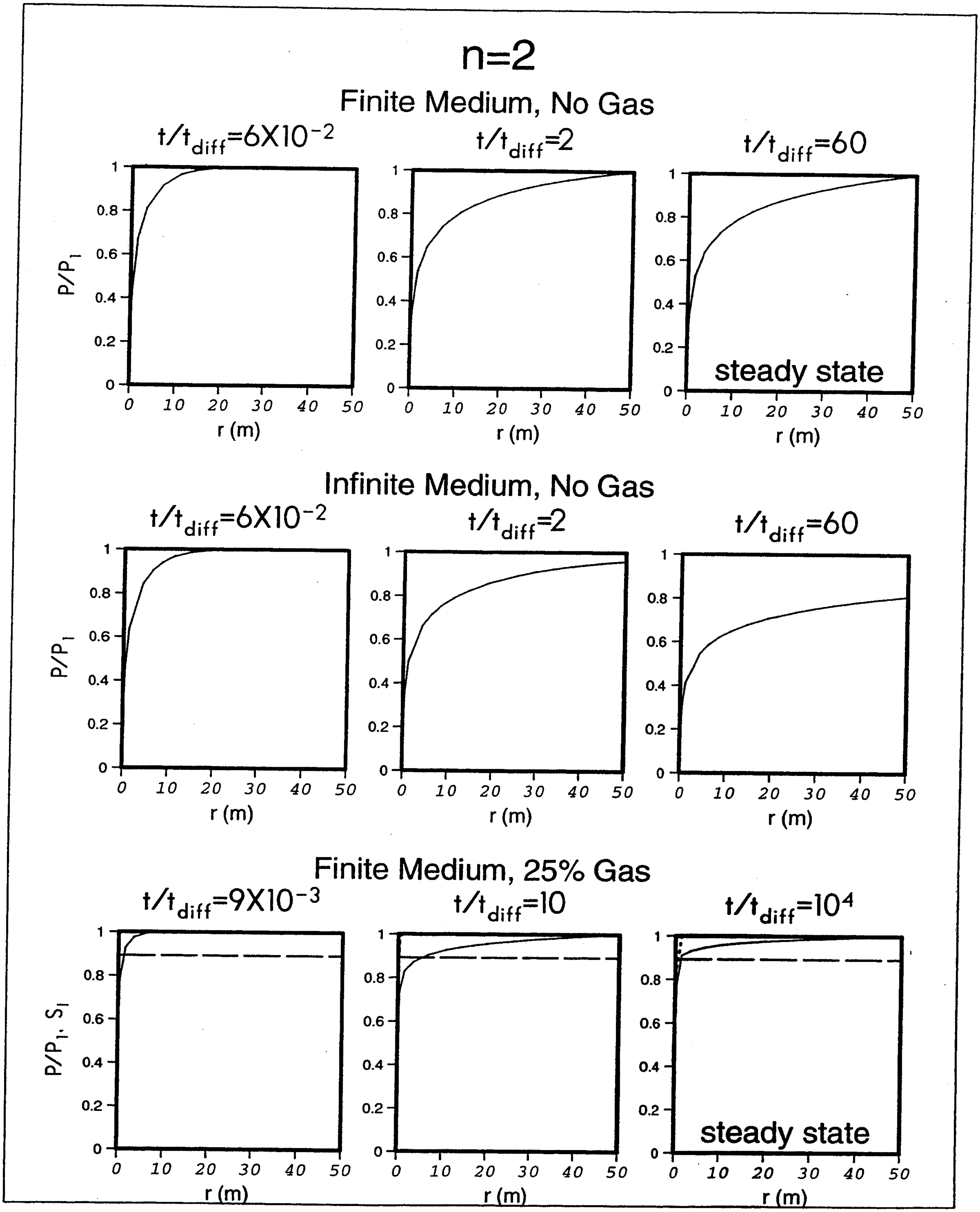
n=2
Finite Medium, No Gas
t/t_diff=6X10^-2
t/t_diff=2
t/t_diff=60
P/P_1
steady state
r (m)
Infinite Medium, No Gas
t/t_diff=6X10^-2
t/t_diff=2
t/t_diff=60
P/P_1
r (m)
Finite Medium, 25% Gas
t/t_diff=9X10^-3
t/t_diff=10
t/t_diff=10^4
P/P_1, S_l
steady state
r (m)

Figure III.6

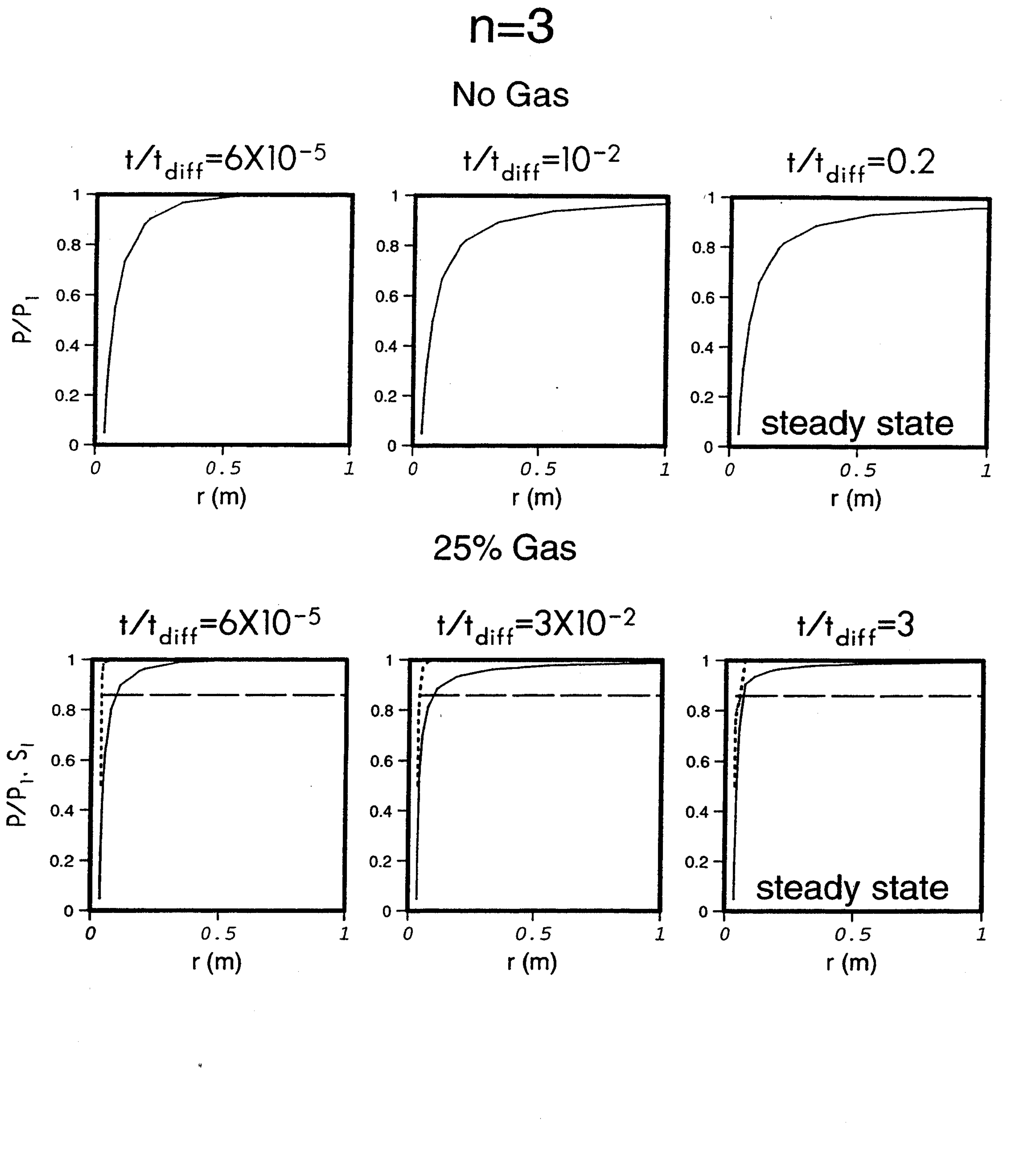
n=3
No Gas
t/t diff=6X10-5
t/t diff=10-2
t/t diff=0.2
steady state
P/P1
r (m)
25% Gas
t/t diff=6X10-5
t/t diff=3X10-2
t/t diff=3
steady state
P/P1, S1
r (m)

Figure III.7

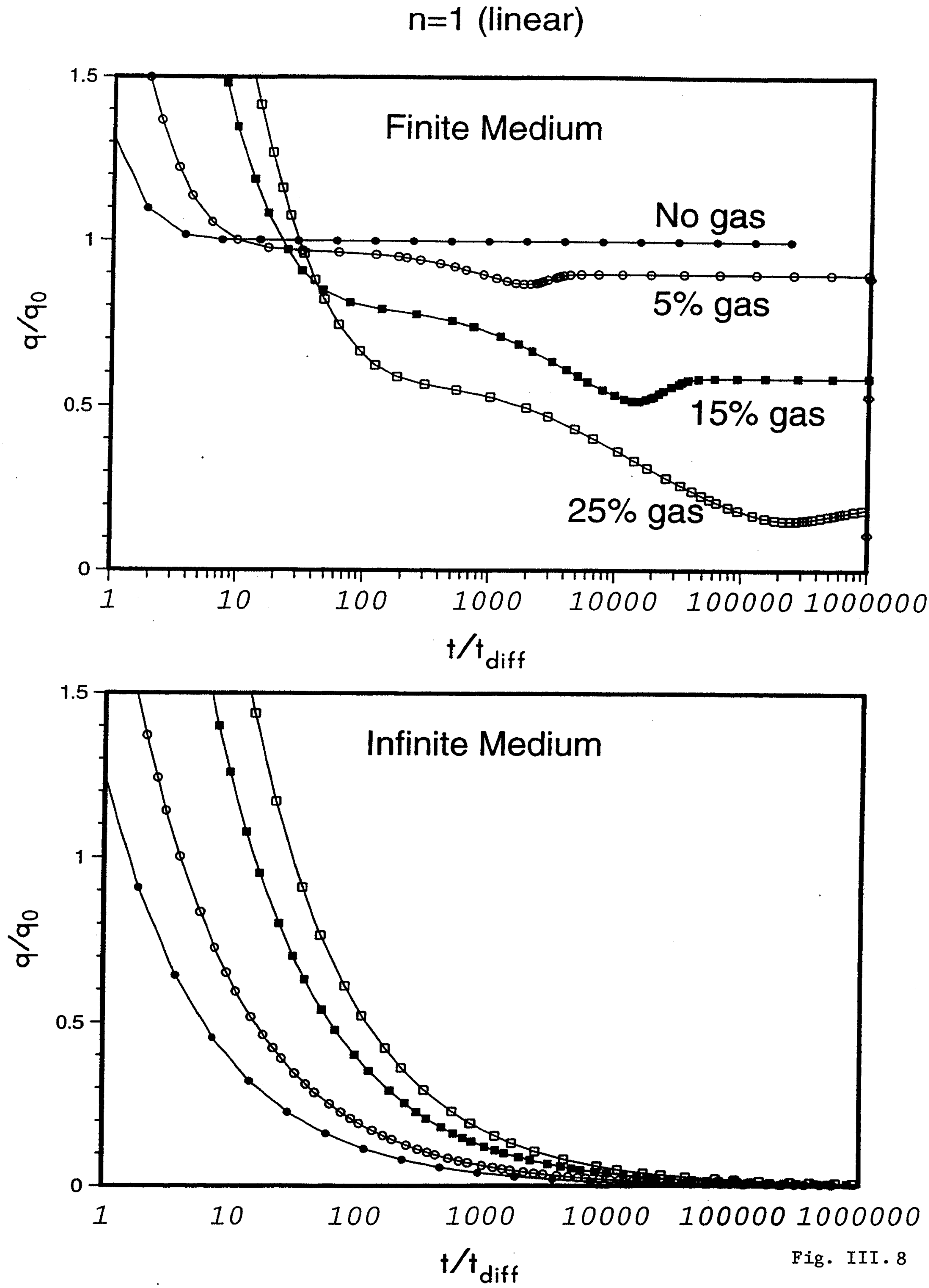

n=1 (linear)
Finite Medium
No gas
5% gas
15% gas
25% gas
q/q0
t/tdiff
1.5
1
0.5
0
1
10
100
1000
10000
100000
1000000
Infinite Medium

Fig. III.8

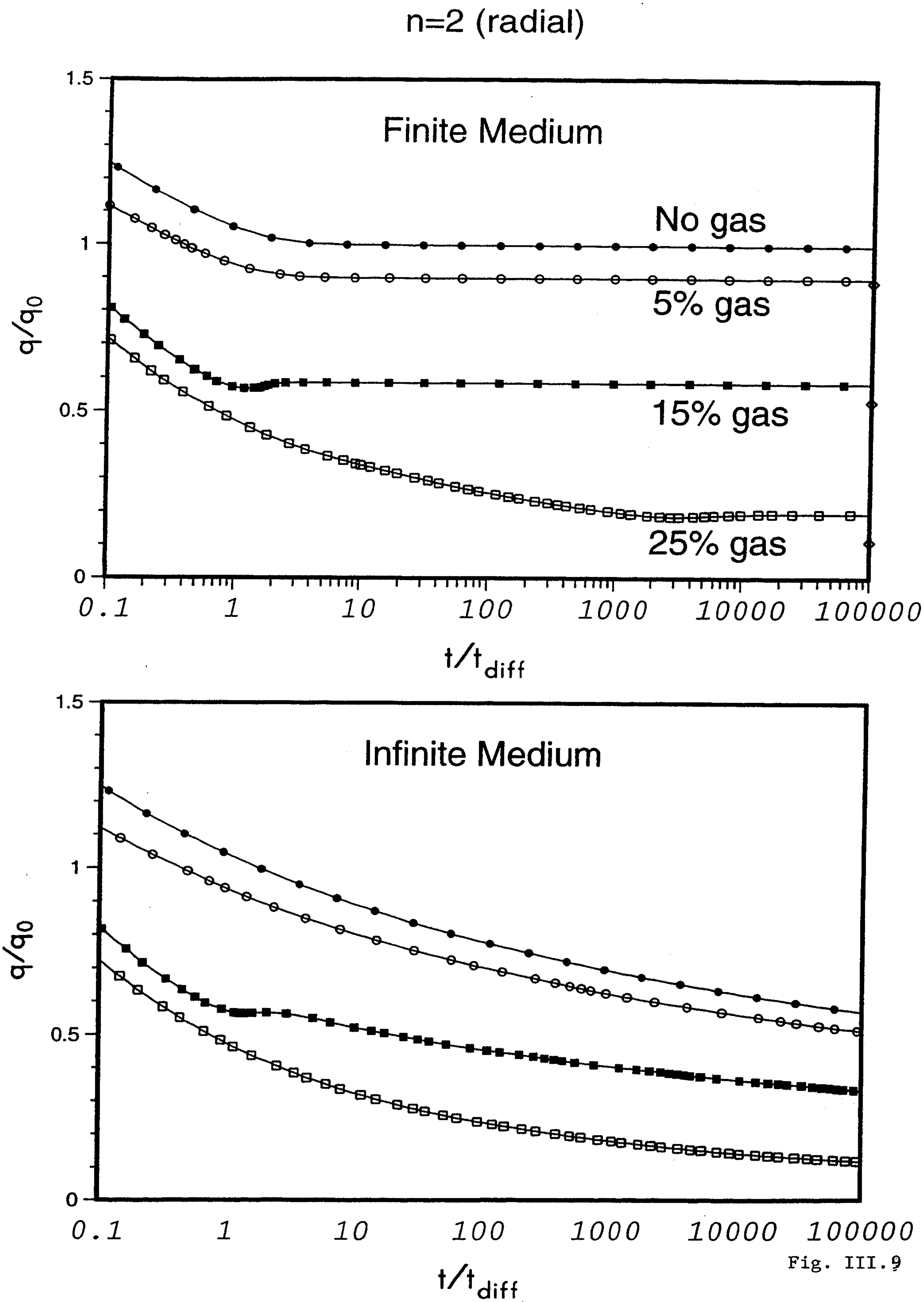
n=2 (radial)
Finite Medium
No gas
5% gas
15% gas
25% gas
q/q0
1.5
1
0.5
0
0.1
1
10
100
1000
10000
100000
t/tdiff
Infinite Medium
q/q0
1.5
1
0.5
0
0.1
1
10
100
1000
10000
100000
t/tdiff

Fig. III.9

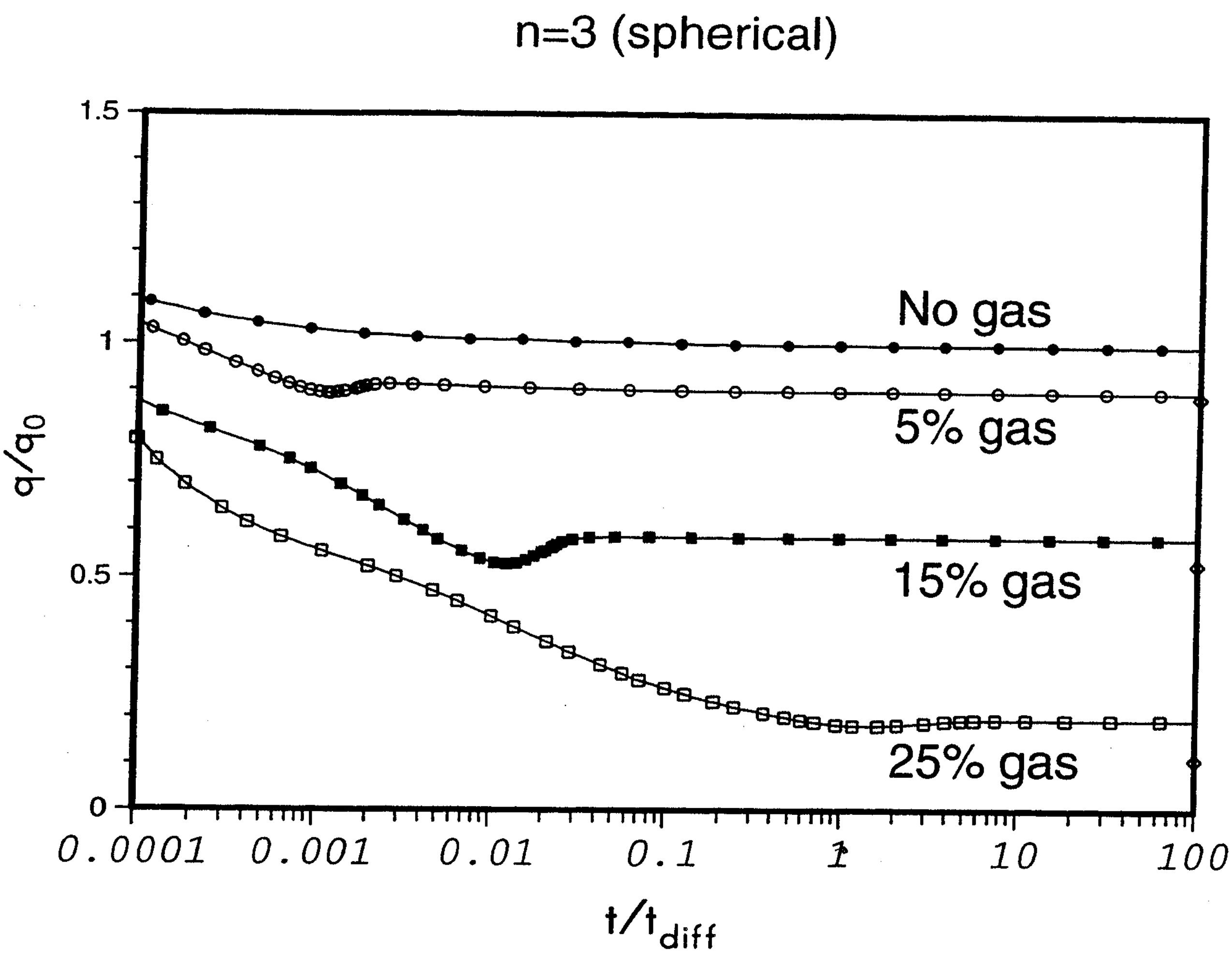

Figure III.10

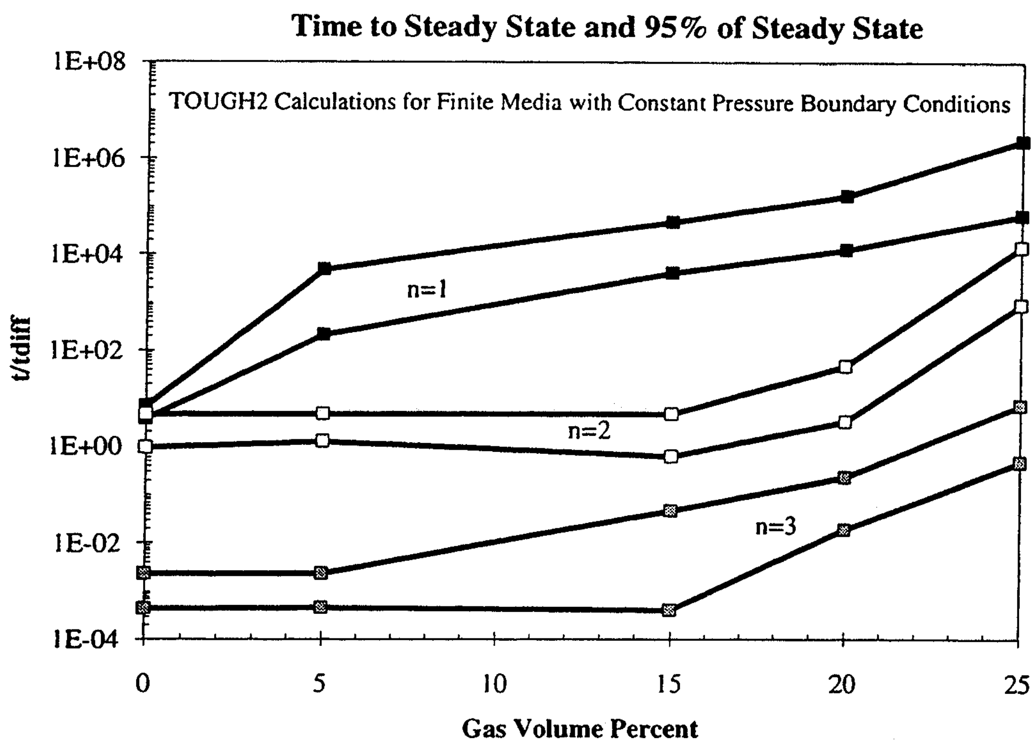

Figure III.11

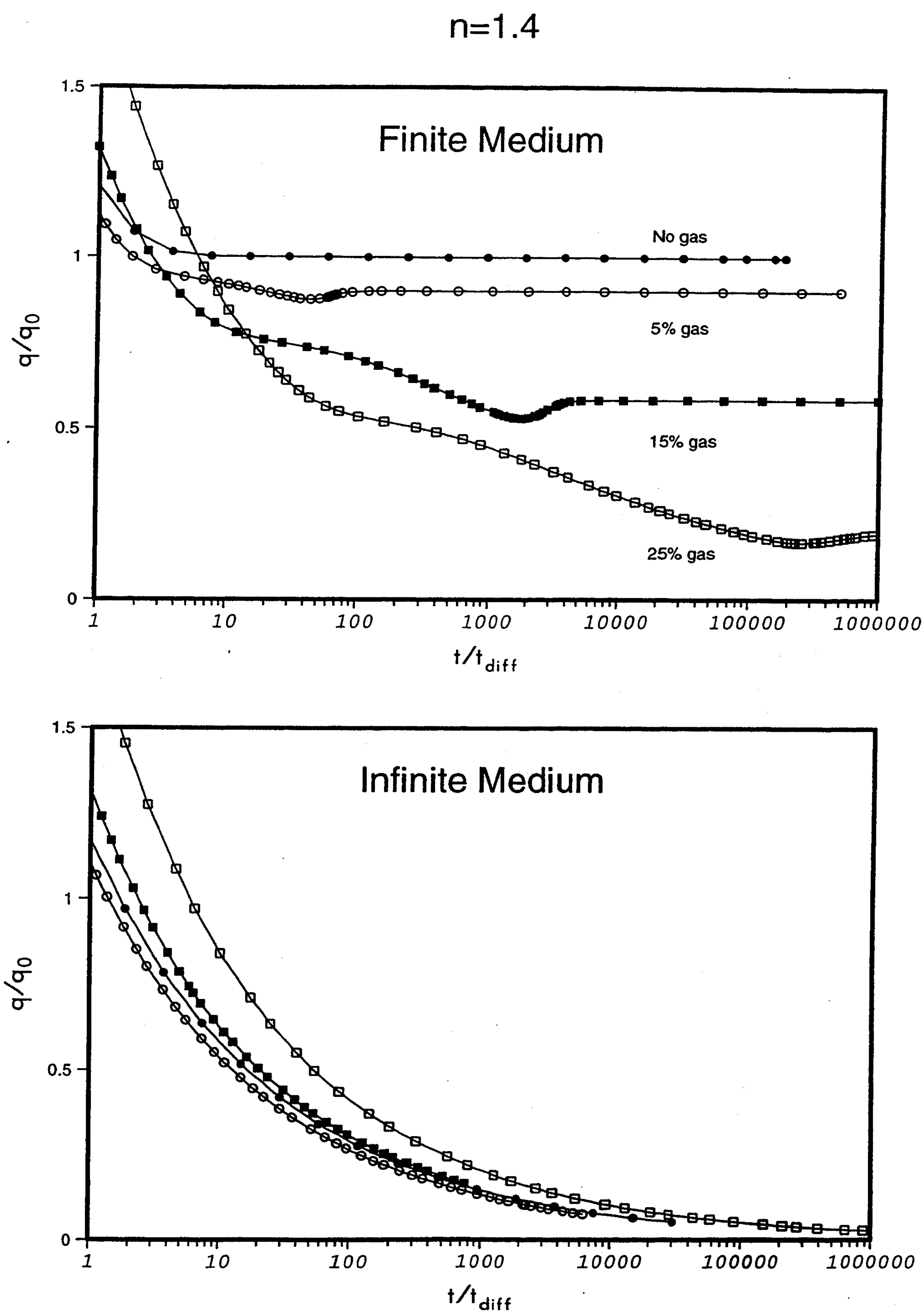

Figure III.12

n=2.4

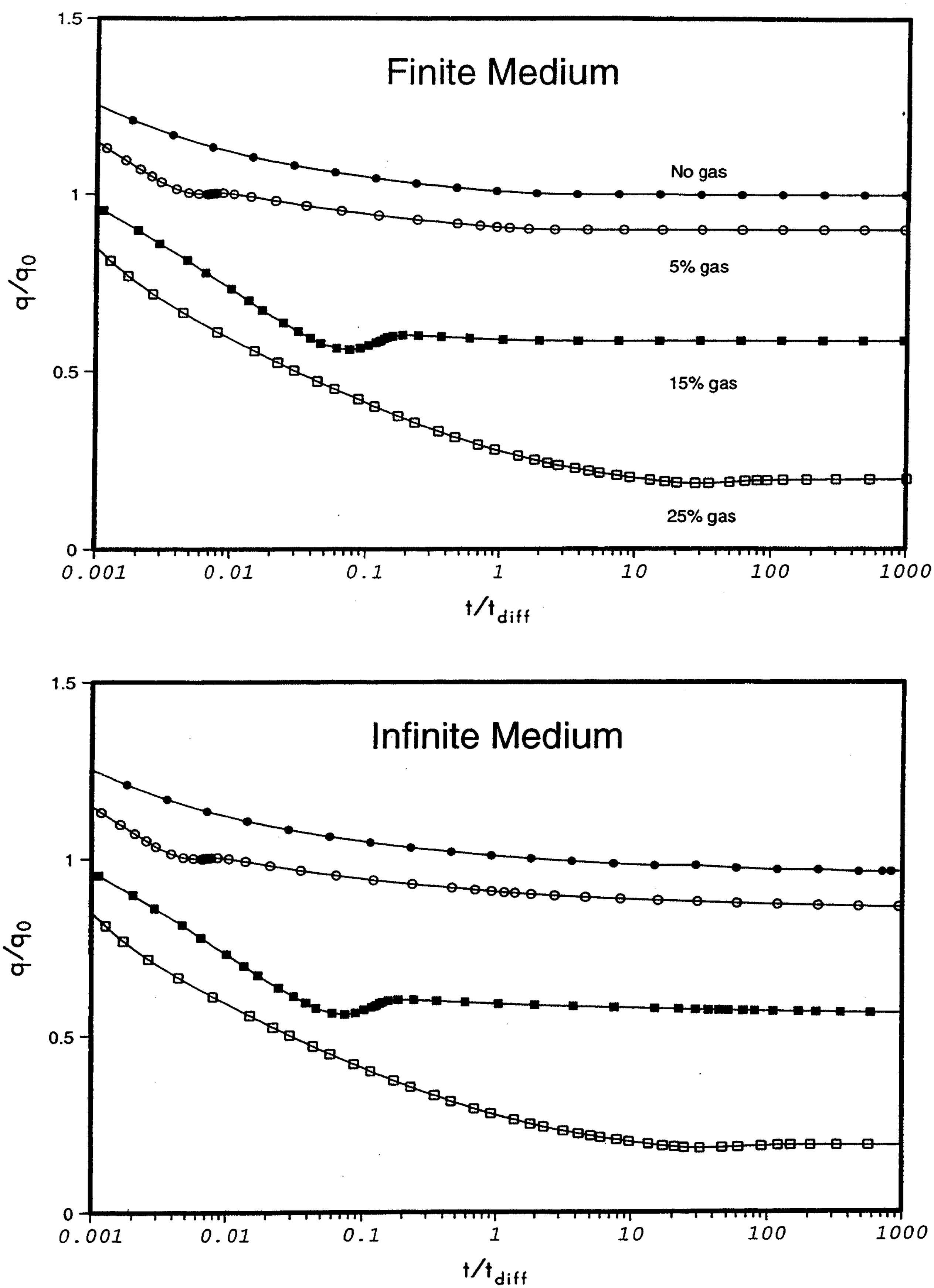

Figure III.13

Dixie Valley Fracture

41 X 41 resolution of aperture distribution, 5 levels

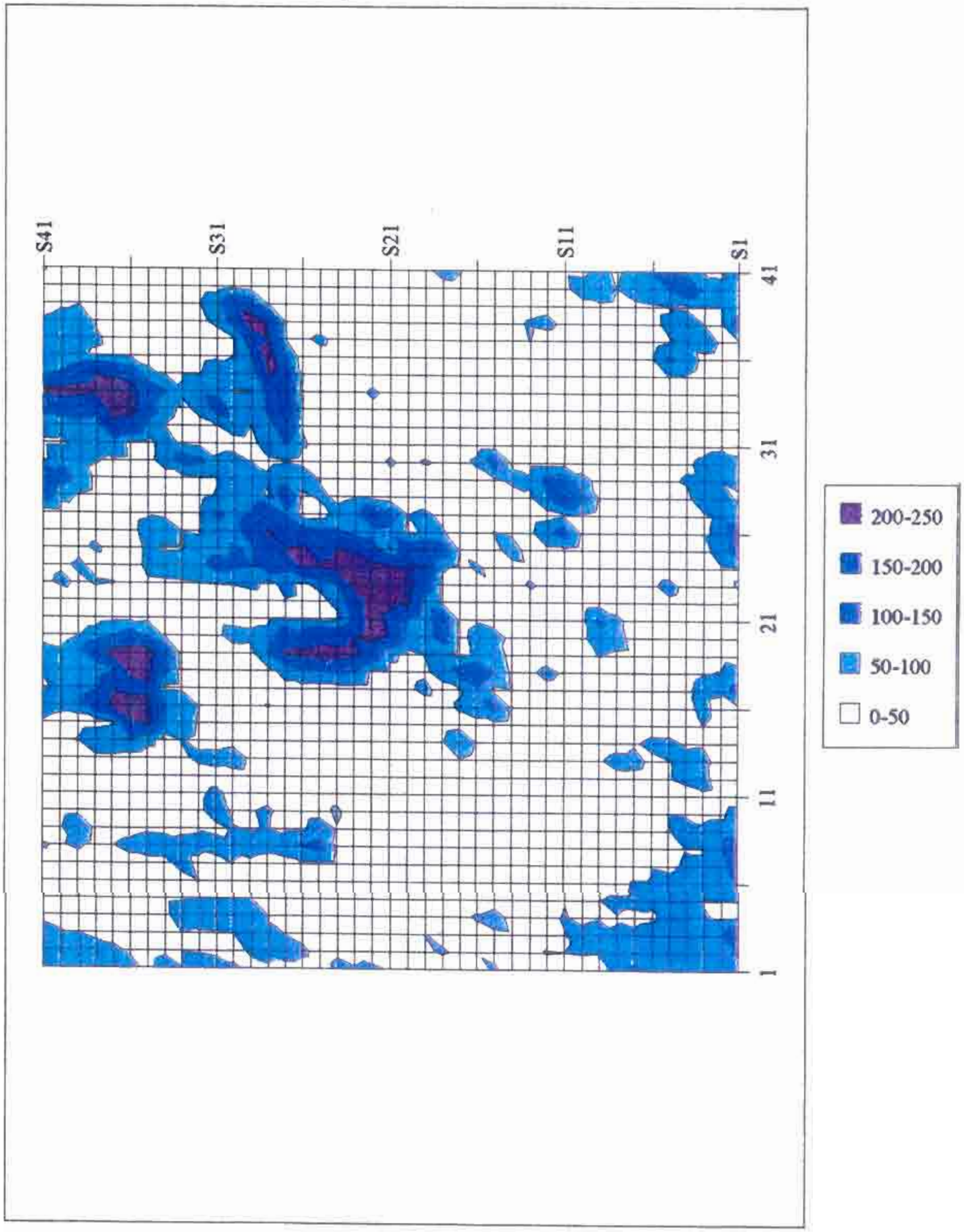

Figure III.14

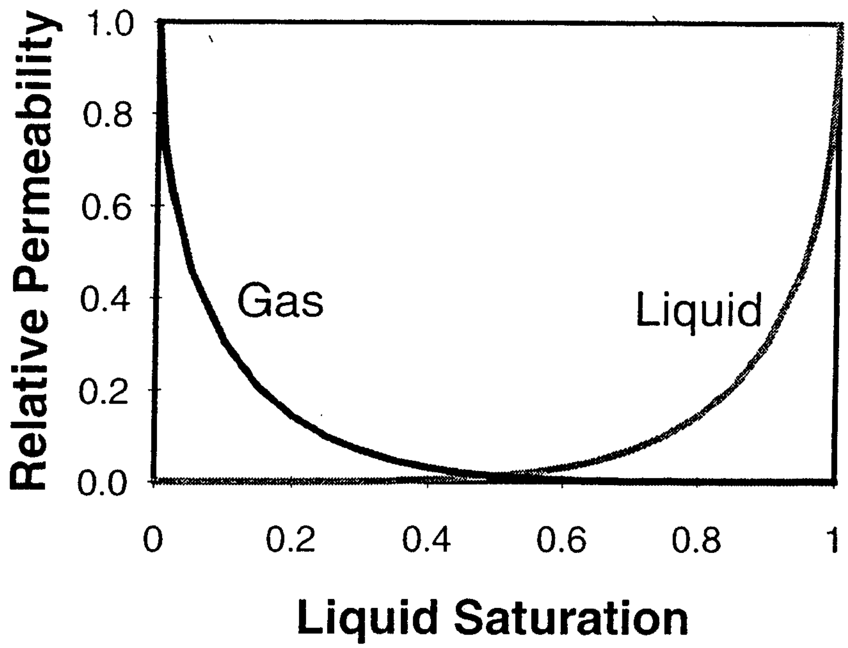

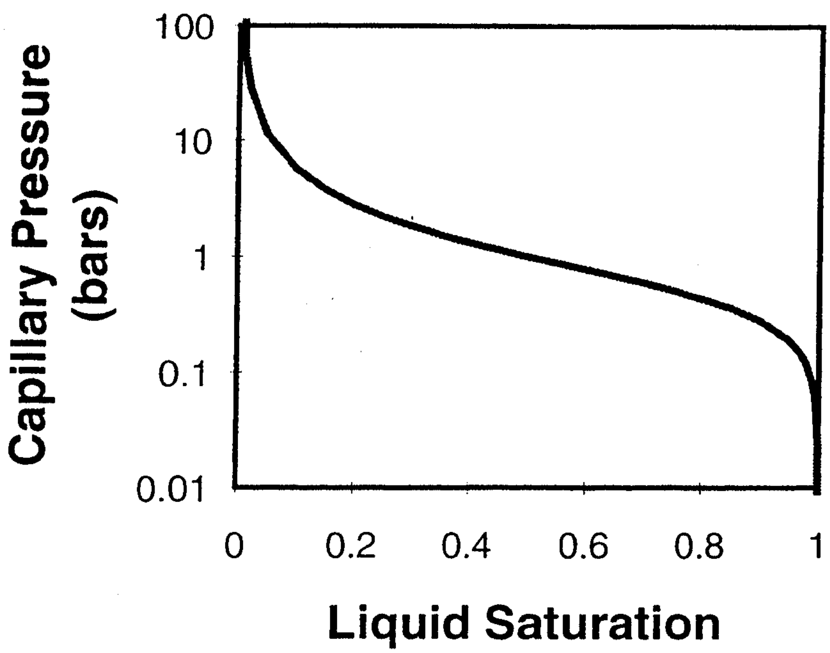

Figure III.15

Dixie Valley Fracture

Pressure Distribution | Gas Saturation Distribution

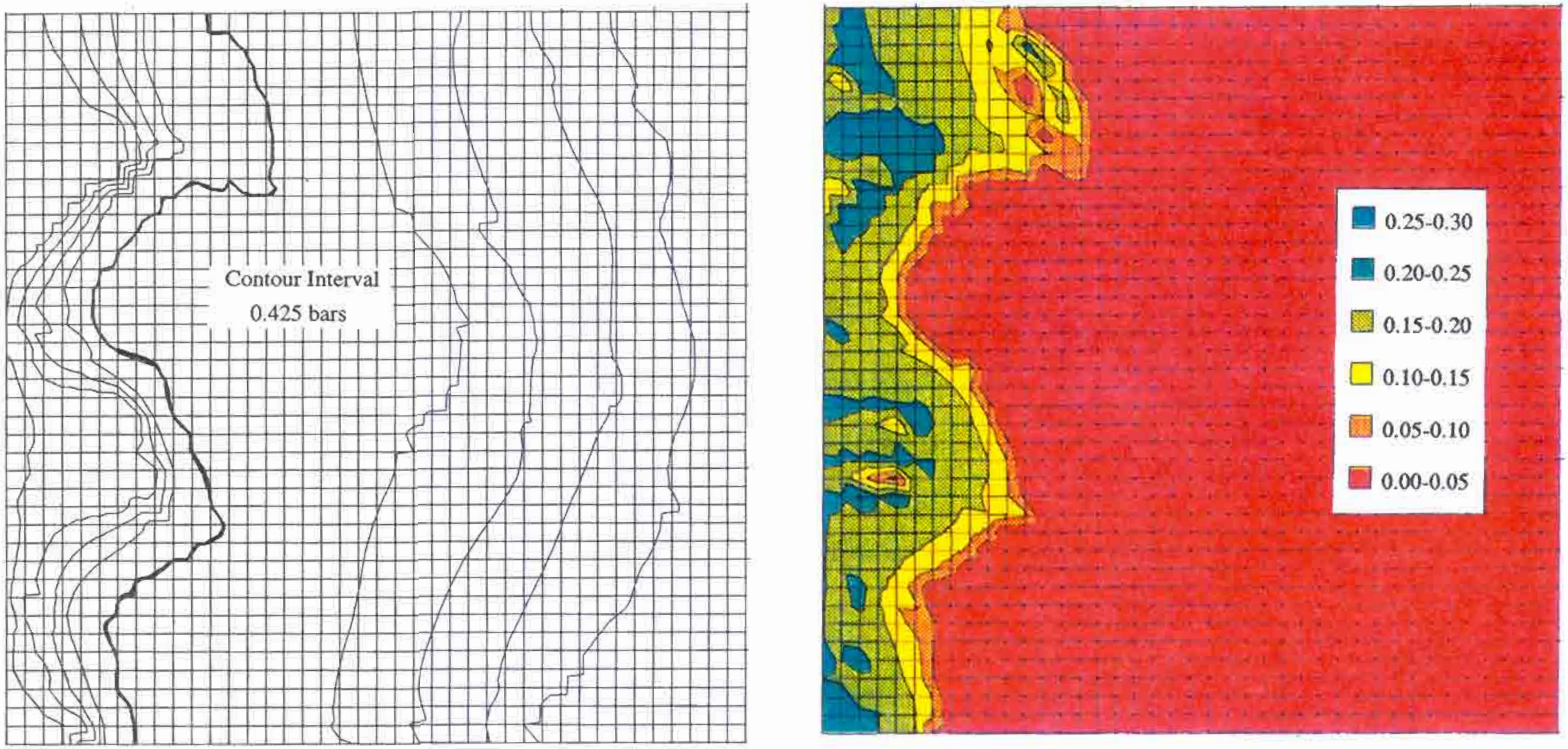

Figure III.16

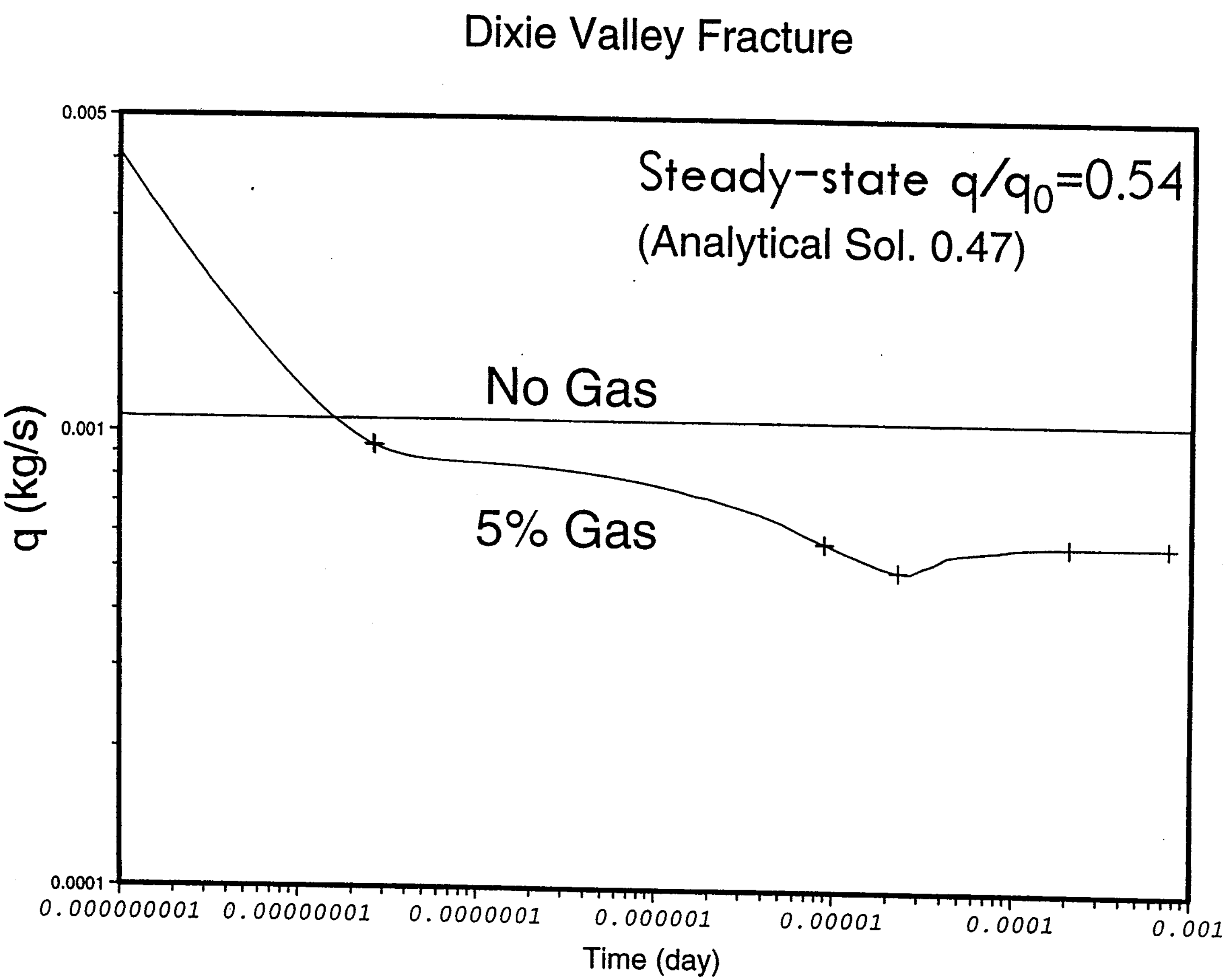

Figure III.17

Dixie Valley Fracture

41 X 41 resolution of small-aperture distribution

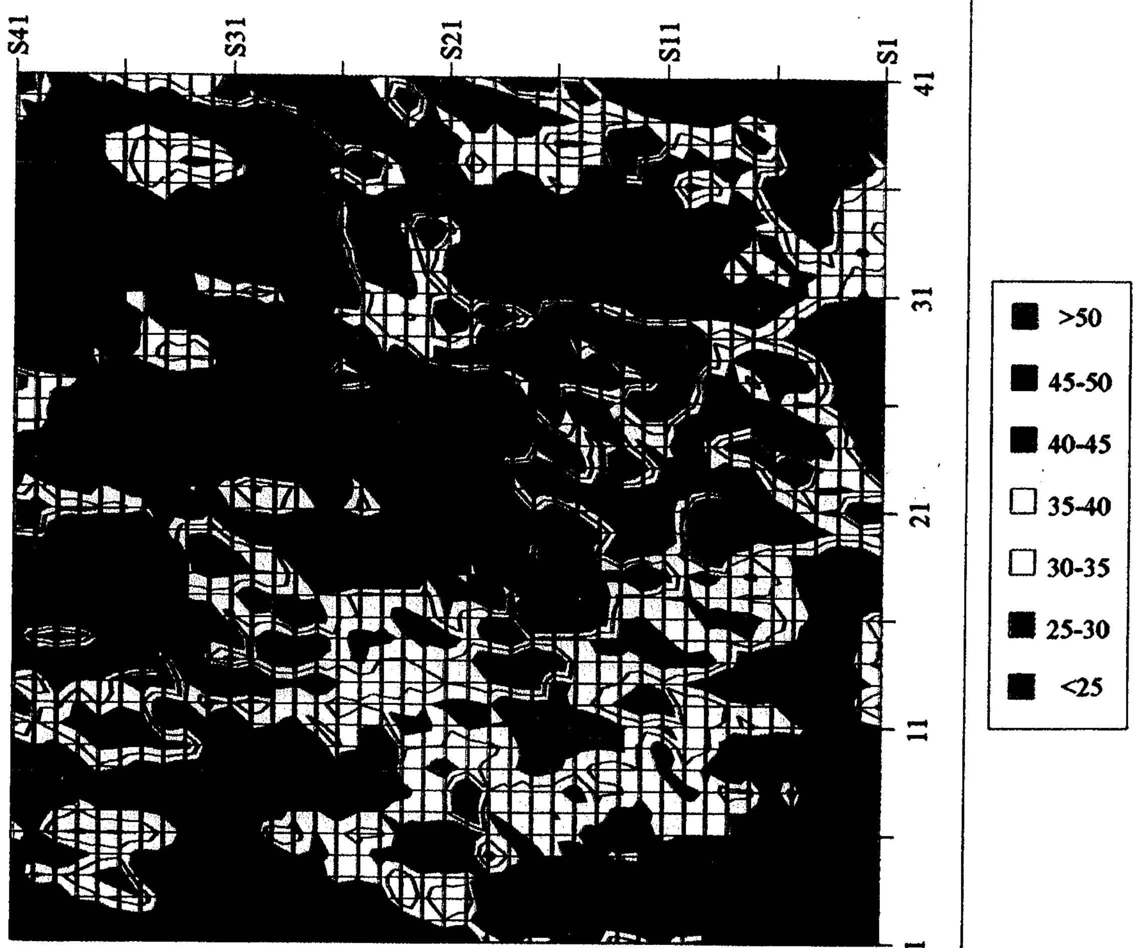

Figure III.18

Dixie Valley Fracture

41 X 41 resolution of small-aperture distribution

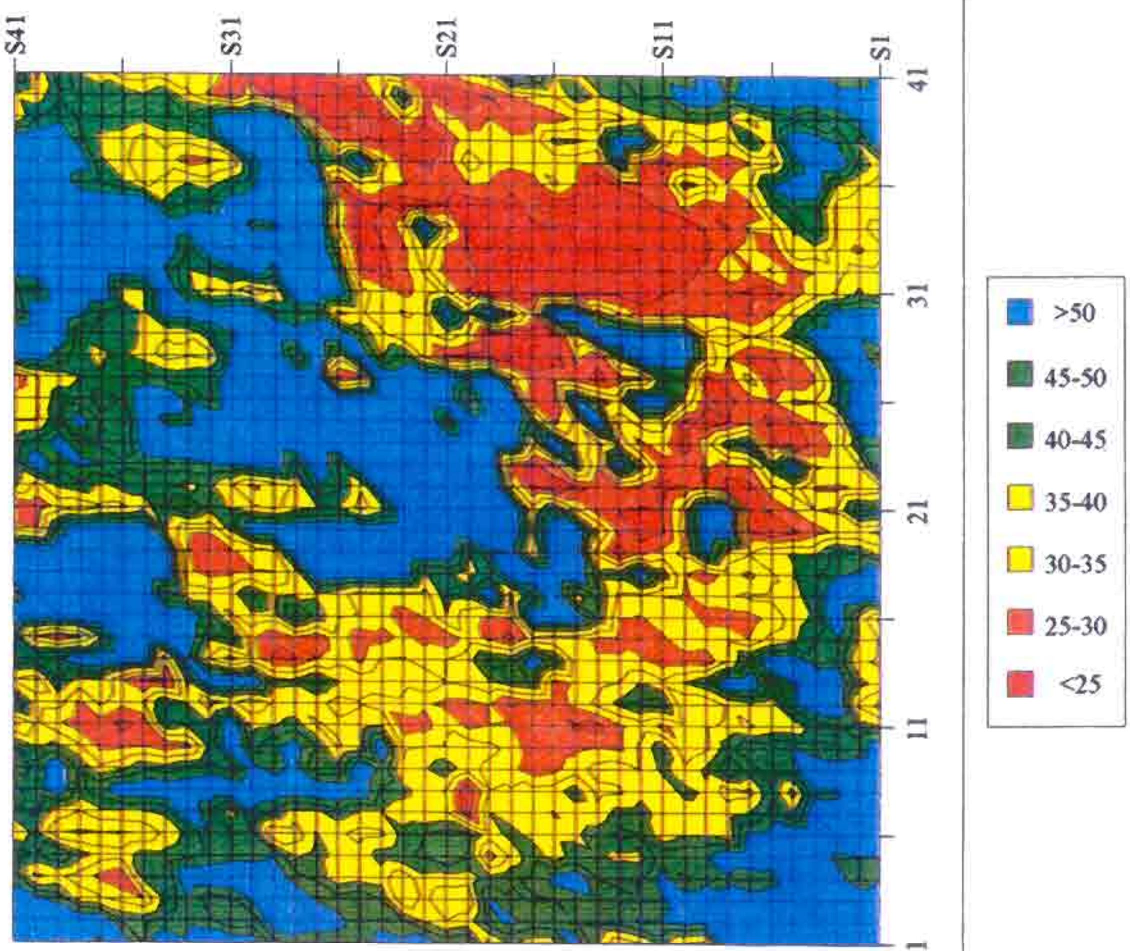

Figure III.18

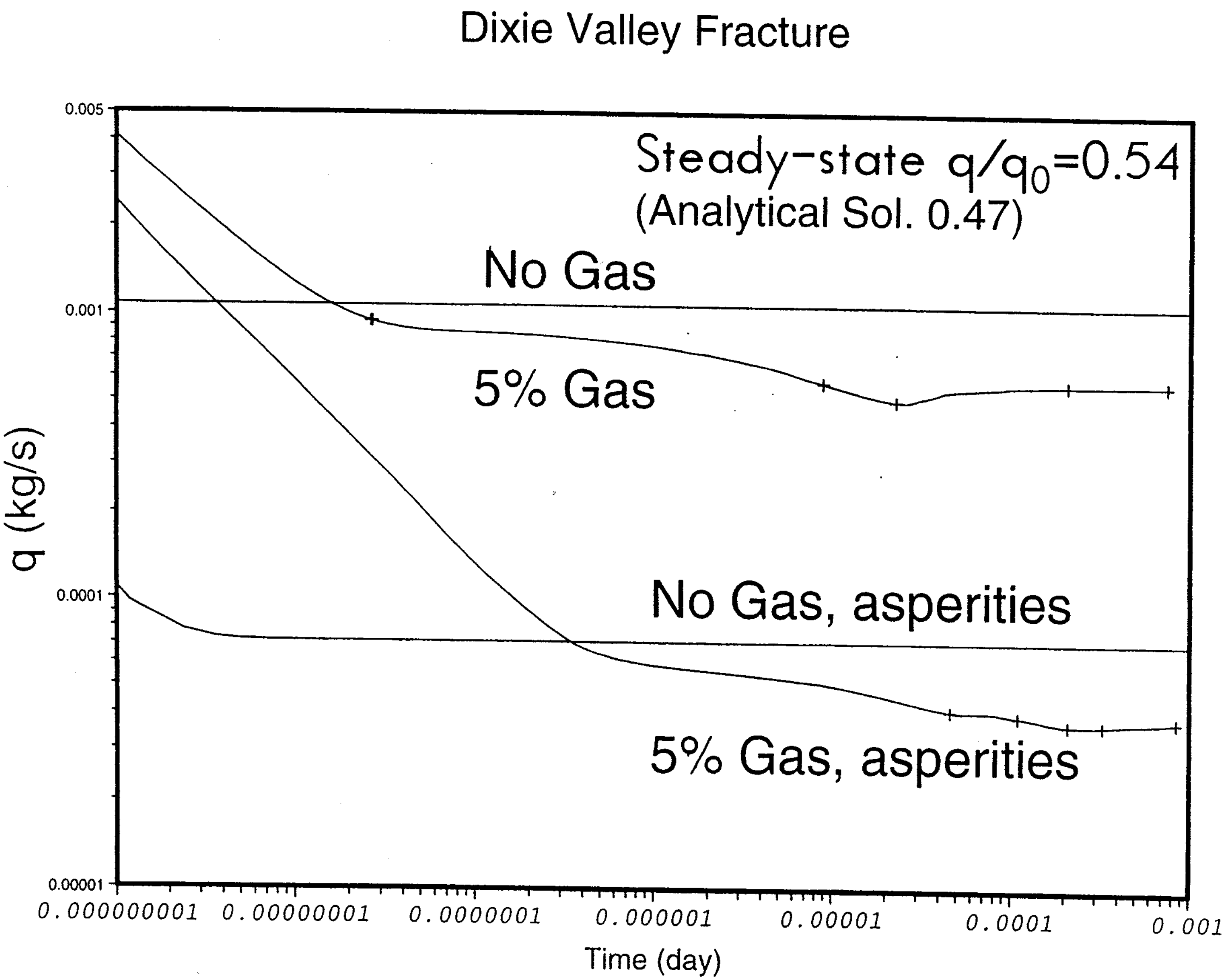

Figure III.19

Dixie Valley Fracture with Asperities

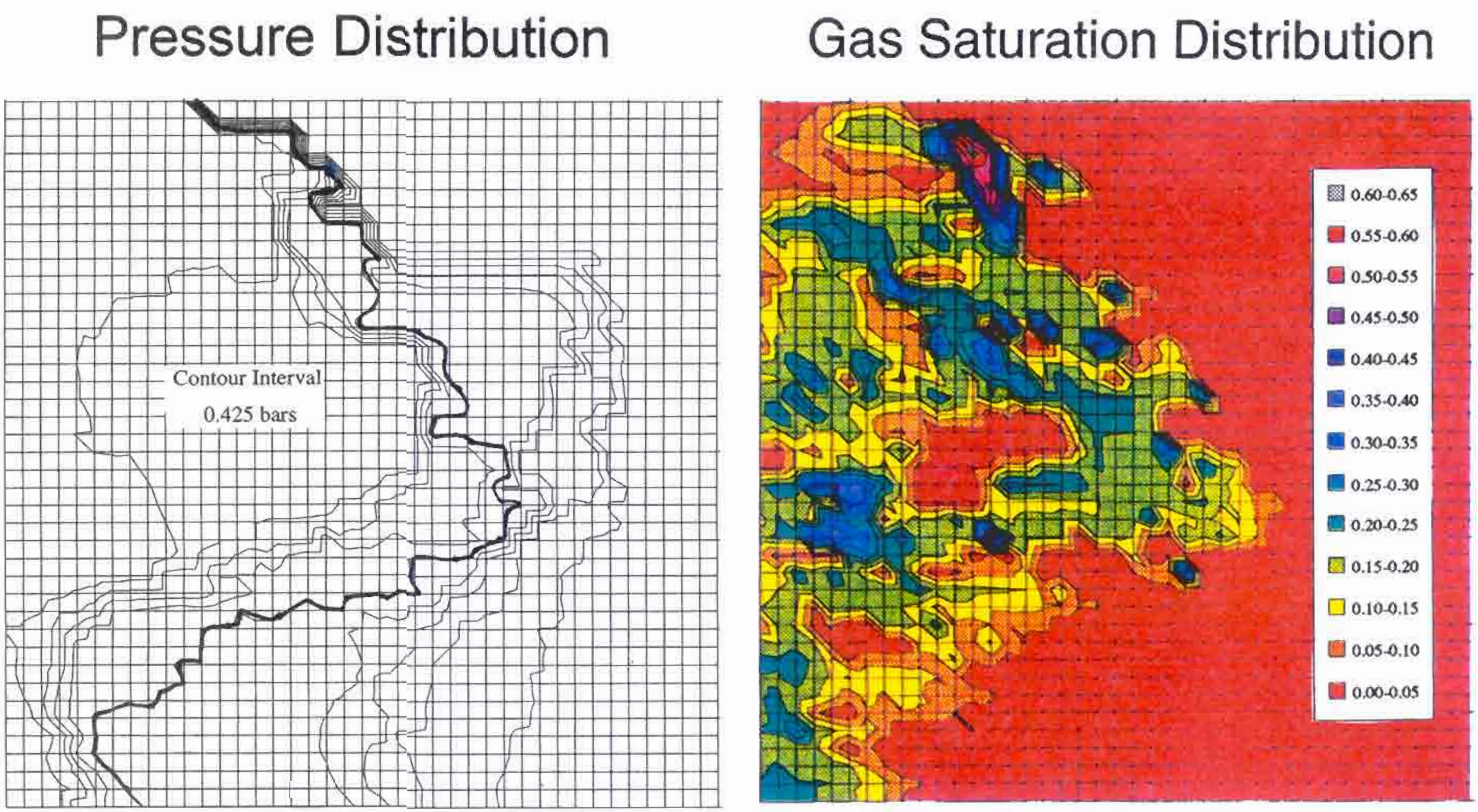

Figure III.20

Dixie Valley Fracture with Asperities

Steady-state Mobility Distribution

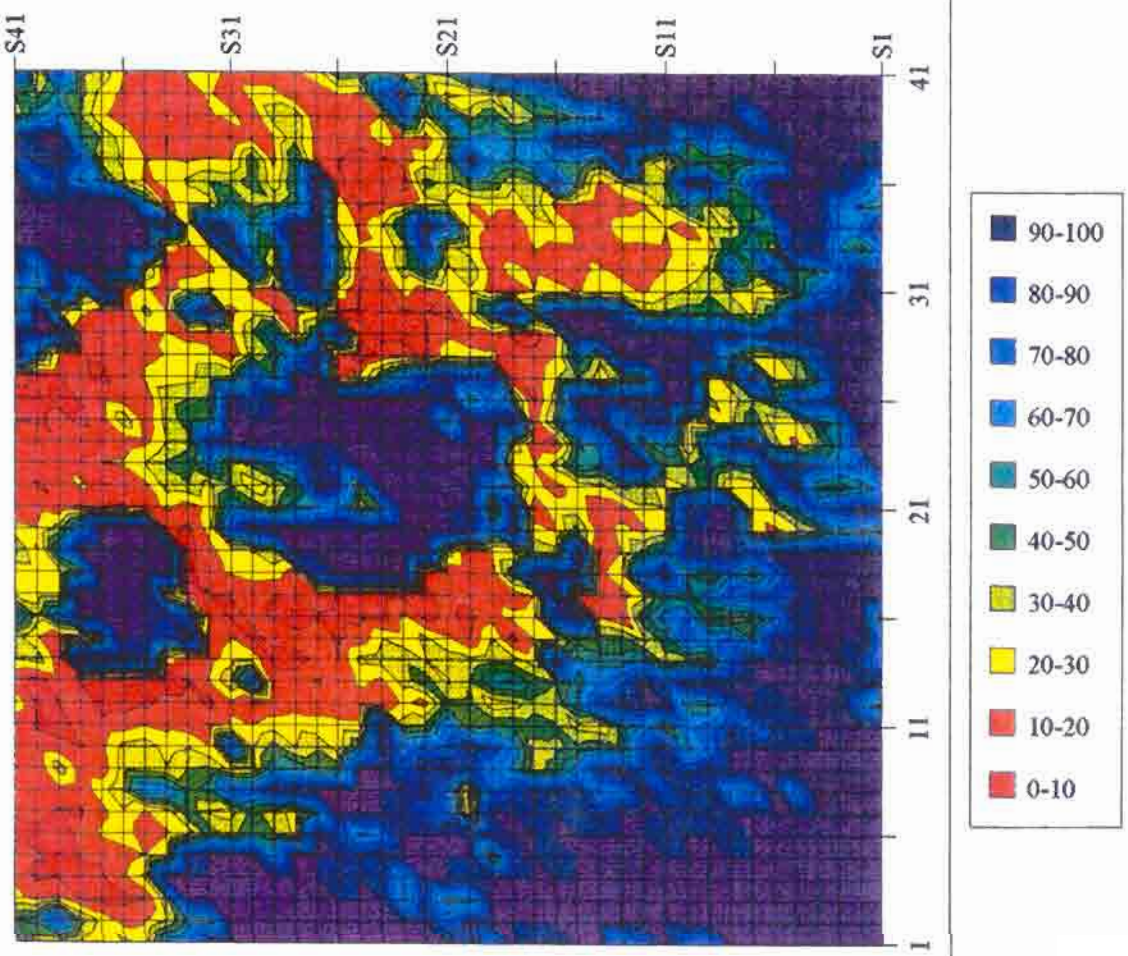

Figure III.21

Dixie Valley Fracture With Asperities

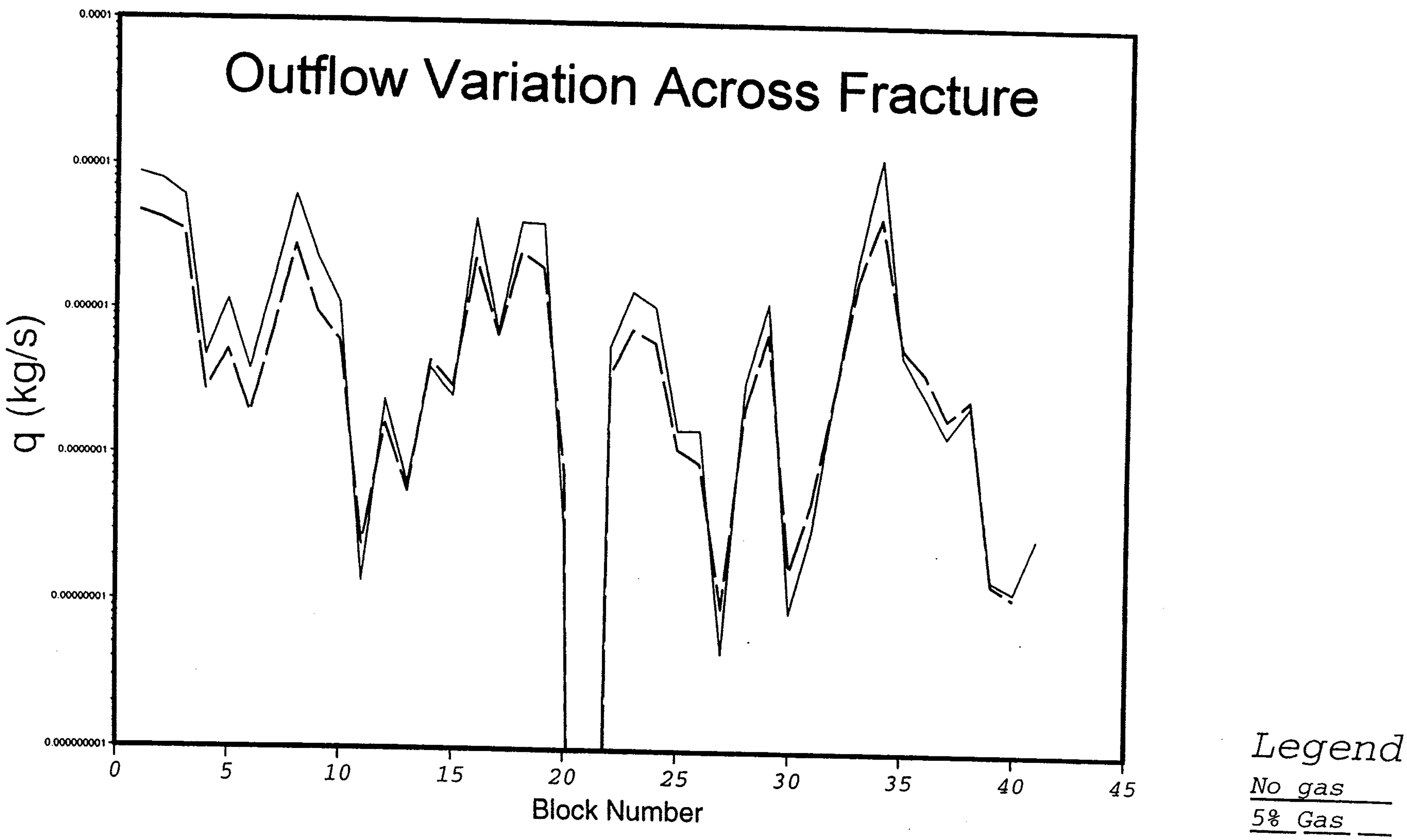

Figure III.22

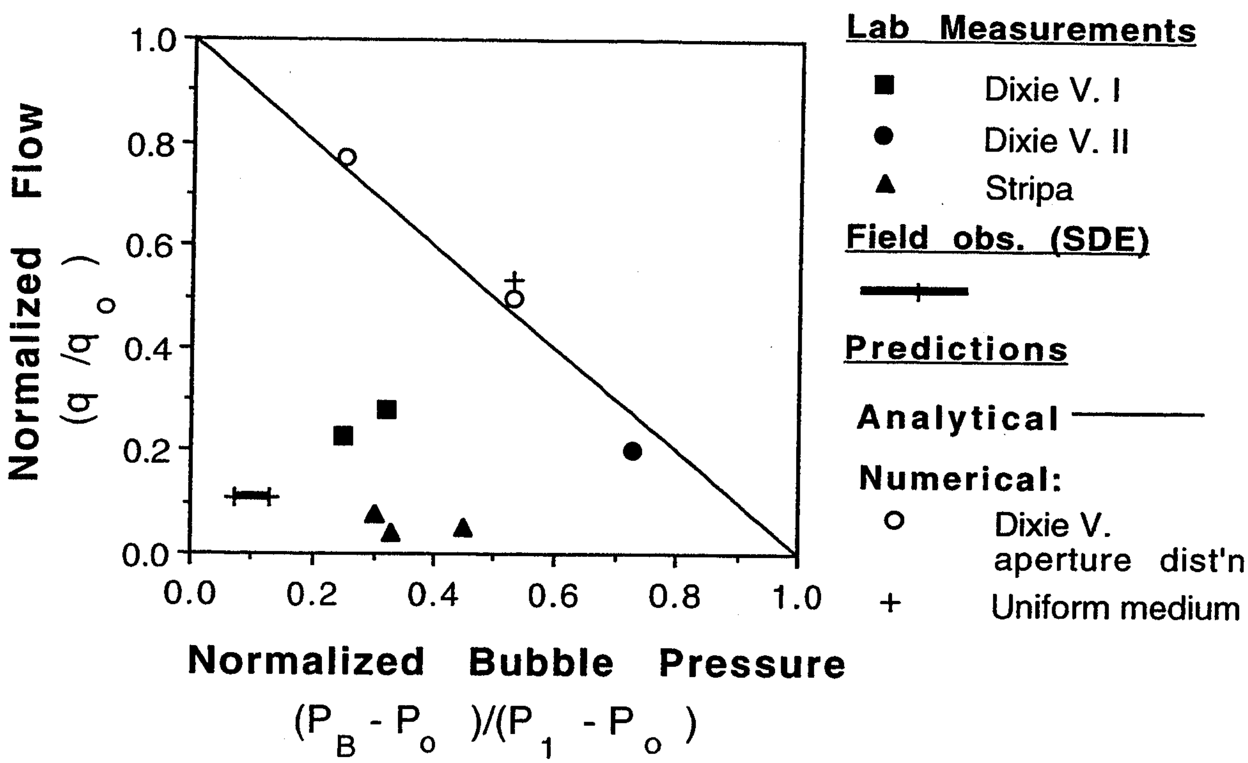

Figure III.23

Two-Phase Flow and Excavation Effects

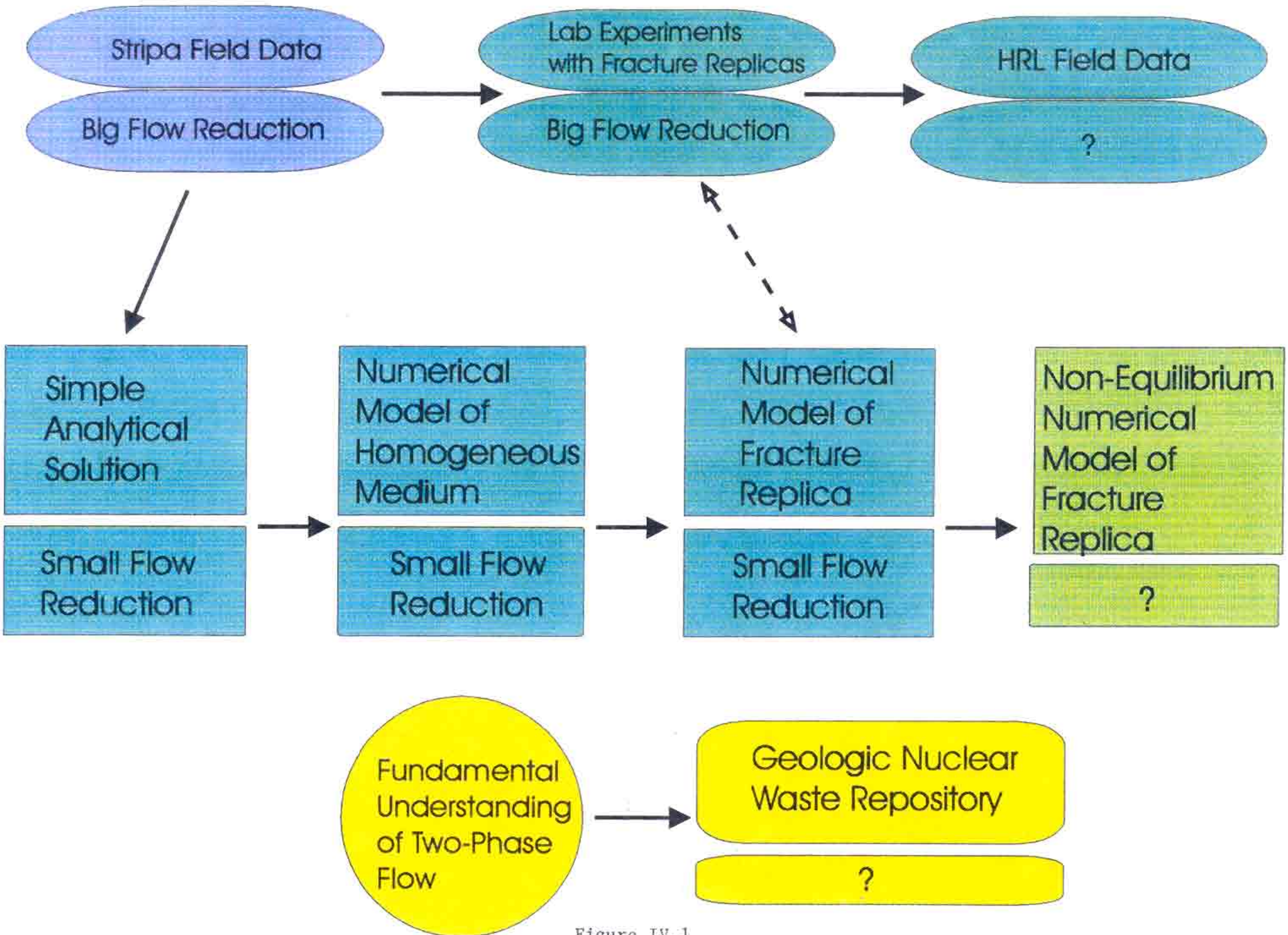

Figure IV.1